Chapter 6
Computed Tomography

Many of the early developments of X-ray-based computed tomography (CT) go back to the pioneering work of Cosslett and Nixon [1–4]. The method of computed tomography is understood as any computer-aided tomographic process (usually involving X-rays) to produce 3D representations of the scanned object both externally and internally. This inspection method has been substantially improved since its technological beginnings in the 1970s and allows inspecting fiber reinforced composite materials nowadays with remarkable precision. Some of the key uses for industrial CT scanning involve flaw detection, failure analysis, metrology, assembly analysis, and reverse engineering applications [5]. X-ray-based computed tomography is an established technology, which is readily available from commercial companies. Consequently, the focus of this chapter is not to cover all fundamentals of the measurement method but its application and limitation in the context of defect sensing in fiber reinforced materials. For a more detailed review on the method of computed tomography, the reader is instead referred to some recent books on this topic [6–8].

To start with the chapter, first an overview on the principle of operation of CT is provided, and some basic configurations of CT are presented. The subsequent section has its focus on the present limitations in terms of CT resolution, including artifacts and typical failure modes as encountered in fiber reinforced materials. One section is used to review the important concepts involving combinations of mechanical loading of materials with CT imaging. As further development of DIC methods, the important aspect of digital volume correlation (DVC) and its application to fiber reinforced materials are discussed. Finally some applications of CT to assess the failure progression in composite materials along with possibilities to use CT information in modeling approaches are presented.

M.G.R. Sause, *In Situ Monitoring of Fiber-Reinforced Composites*,
Springer Series in Materials Science 242, DOI 10.1007/978-3-319-30954-5_6

6.1 Principle of Operation

A conventional X-ray inspection is based on a simple projection of the test object onto a detector using a point-like X-ray source. This simple geometrical arrangement as seen in Fig. 6.1 causes a projection of the object volume to the detector and has been termed "shadow microscopy." The magnification factor of the test object is primarily determined by the distance between source and object as well as the distance between the object and the detector.

In order to yield a difference in detected X-ray intensity, two main effects can be distinguished:

1. The detected intensity may be decreased due to a material with higher X-ray absorption.
2. The detected intensity may be decreased due to a test object with higher thickness.

Hence, one projection direction may not allow to distinguish between both effects, since a reduction in detected X-ray intensity could be due to either effect or a combination of both.

In contrast to the conventional 2D projection, the process of CT uses projections of the test object acquired at different angles and combines their information to yield a volumetric structure of the test object. This is only possible by usage of a reconstruction algorithm operating on discretized versions of the projection images.

The typical CT configuration basically requires three components, an X-ray source, a moveable table carrying the test object, and a detector system. Although there are many types of CT configurations available, only the most common type of cone-beam CT will be explained in the following, since it was used for the experimental results shown in this chapter.

For a CT scan, the test object is placed on a rotary table. Similar to the principle of "shadow microscopy," in CT the test object can be moved closer to the source to yield higher magnification or closer to the detector to yield lower magnification. One very important factor for cone-beam CT is that the part must fit in the field of view of the detector to allow proper reconstruction (Fig. 6.2). After the initial alignment, the test object is rotated 360° and 2D X-ray projections are taken at

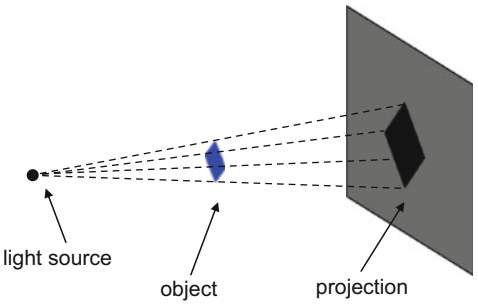

Fig. 6.1 Arrangement of source, test object, and detector in "shadow microscopy"

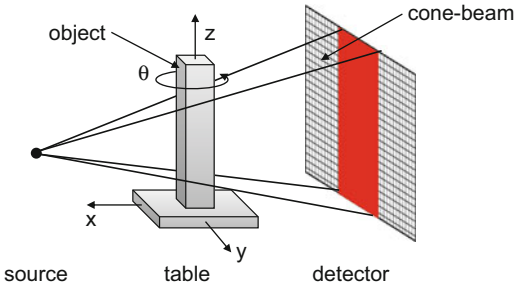

Fig. 6.2 Typical arrangement of cone-beam CT

distinct angles. For typical CT acquisitions, the number of X-ray images ranges from several hundreds to several thousands in a single rotation of the test object. The individual images are then reconstructed to create a 3D volume representation of the test object. If the test object does not allow a full 360° rotation, special reconstruction algorithms are used to allow scans based on projected images acquired at fractions of the full 360° rotation.

In the following, some key aspects of CT are discussed in more detail to allow a better understanding on how the X-ray source, the detector, and the reconstruction algorithm influence the imaging process. In the context of this book, the main application is to visualize the interior volume of fiber reinforced materials.

In order to improve the resolution of X-ray microscopes, one of the key challenges was to achieve a smaller source size, while keeping or increasing the brightness of the source to allow for reasonable exposure times. This lead to the geometrical arrangement of X-ray tubes nowadays referred to as micro-focus or nano-focus tubes as seen in Fig. 6.3 which constitute the most frequently used X-ray source.[1]

As with any conventional X-ray tube, the first step is a generation of a free electron gas using thermionic emission by a heating voltage U_H applied to a coil located inside a vacuum tube. The free electrons are focused to leave a filament grid and form an electron beam using a voltage U_G. By using an acceleration voltage U_{acc} between the emission coil and an anode, the electron beam is further accelerated and directed towards a target material. The target material (typically tungsten or molybdenum) is hit by the electron beam, and X-rays are released in form of deceleration radiation and characteristic radiation. To achieve a high resolution, a small focal spot size and thus a small interaction volume between electron beam and target material are necessary. In order to minimize the focal spot size, the electron beam is typically focused using magnetic lens systems minimizing its cross-section at the position of target impact. In addition, high-resolution tube systems use target materials, which are comparatively thin and are arranged perpendicular to the incident beam (transmission tubes). This is in contrast to the usual

[1] In principle, radioisotopes could also be used to generate 2D projections of objects as frequently done in field applications. However, the handling aspects and the intensity decay of these sources practically inhibit their use for computed tomography applications.

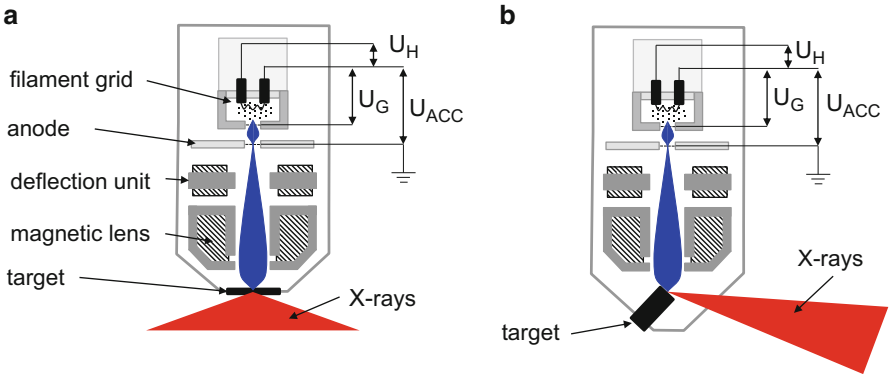

Fig. 6.3 Configurations of X-ray transmission tubes (**a**) and tubes using directional design (**b**)

configuration with oblique incidence of the electron beam onto a thick target material, a configuration which is known as directional tubes. In any case the X-rays are released within the target material and radiate outward from their position. This causes a typical cone-shaped X-ray beam spreading starting at the source spot.

A superior technological alternative as an X-ray source for CT is synchrotron radiation. When electrons traveling at ultrarelativistic speeds are forced by a magnetic field to travel in a curved path, synchrotron radiation is produced. In theory, the ultrarelativistic speed will change the observed radiation frequency due to the Doppler effect. The relativistic length contraction changes the radiated frequencies further, thus effectively yielding electromagnetic radiation in the X-ray spectrum. The radiation pattern can be distorted from an isotropic dipole pattern into an extremely forward-pointing cone of radiation depending on the velocity of the electrons. Synchrotron radiation is the brightest artificial source of X-rays and may be achieved artificially in synchrotrons or storage rings. The electromagnetic radiation produced in this way has a characteristic polarization, and the high intensity photon beam allows fast exposure times for CT scanning. In addition, the high brilliance of the synchrotron beam generates a small divergence and enables a small source spot size.

Another important component to achieve high-resolution volumetric representation of objects is the detector system. For computed tomography this is a device that captures X-rays and usually converts them to light in the visible spectrum. Among the most relevant detector concepts used, there are scintillator systems and flat-panel detectors. In practice this includes line scanners and array scanners to produce 1D or 2D projections of the test object.

For the scintillator systems, the incident X-rays are first converted by a scintillator crystal into visible light. A photo cathode is then used to convert the visible light into electrons, which are accelerated and focused onto a fluorescent screen. The projected image on the fluorescent screen is then detected by a CCD camera system and constitutes the final 2D digital image. As technological alternative, the

digital flat-panel detectors use a thin scintillation foil directly applied on a matrix array of photodiodes operating in the range of emitted visible light. The detected photon intensity is then turned into a 2D digital image. Some of the recent developments consider the overall pixel resolution of the detector arrays, which has a direct impact on the detail visibility. In addition, digital detectors come in a variety of pixel pitches which is the space between pixels. Typically a detector with a smaller pixel pitch relates to longer image acquisition time and higher costs and requires a higher photon flux to produce an image. A larger pixel pitch requires less energy to light up the pixels and is cheaper to manufacture but reduces resolution.

As fundamental principle of computed tomography, the 2D projections by itself are meaningless without further processing by a reconstruction algorithm. The task of the latter is the generation of 2D slices transverse to the axis of rotation and the subsequent stacking of these individual slices to produce a 3D volume. The usual algorithm, which is applied to this end, is the filtered back projection, which is based on the Radon transformation developed in 1917 by Radon [9]. Since the ongoing developments in this particular field expand beyond the level of detail intended for this chapter, the interested reader is referred to some recent literature in this area for more precise information [6–8].

6.2 Detail Visibility

Within this section the important aspect of detail visibility is reviewed. The term detail visibility accounts for our perception of the scanned objects. Since this is not equivalent to the system resolution, it needs some further specification. In most of the imaging technologies, detail visibility is used for the (human) ability to identify a certain object as what it is. Thus it can be understood as the necessary resolution of the image in terms of pixels or voxels sufficient to allow spotting a detail, which is different to its surrounding. However, in a general situation, an exact definition of detail visibility is quite challenging, since our perception is substantially influenced on whether the relevant structure is isolated against a background or whether the structure is periodic with a certain grid length. In the context of this chapter, the term will be used in conjunction with the aspect of visualization of defects in fiber reinforced materials. Some examples of CT images are presented at the end of this section to provide a subjective feeling of detail visibility as achieved by the state-of-the art computed tomography devices.

Before, the two main contributions influencing detail visibility are discussed. First, the overall object resolution as well as induced uncertainties of the experimental configuration of the 2D projections is derived. Second, the aspects of image artifacts arising from material combinations, reconstruction algorithms, and other effects are presented.

6.2.1 Object Resolution

Based on the concept of shadow microscopy, the geometrical magnification M is readily derived by the length of the focus-object-distance (FOD) and the length of the focus-detector-distance (FDD) as

$$M = \frac{\text{FDD}}{\text{FOD}} \tag{6.1}$$

This simple geometrical relationship is shown in Fig. 6.4a schematically and as measurement result of a composite material in Fig. 6.5.

In principle, (6.1) would allow arbitrary large magnification factors, given the size of the detector is scaled accordingly. However, the actual object resolution is not just determined by the geometrical magnification factor. To assess the final resolution of the measurement system, there are three contributions from the experimental equipment to take into account:

1. Pixel size $\widetilde{P}$
2. Focal spot size $\widetilde{F}$
3. Mechanical stability

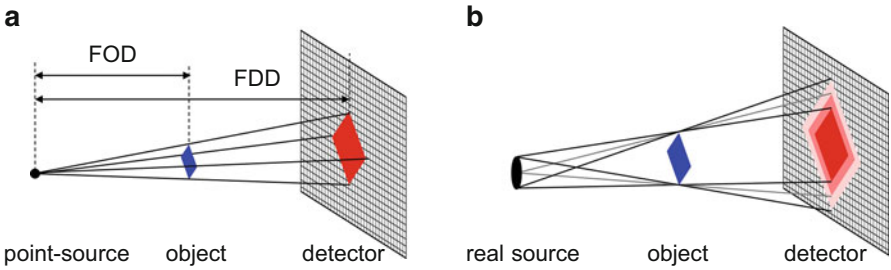

Fig. 6.4 Definition of geometrical magnification factor (**a**) and relation between penumbra effect and focal spot size (**b**)

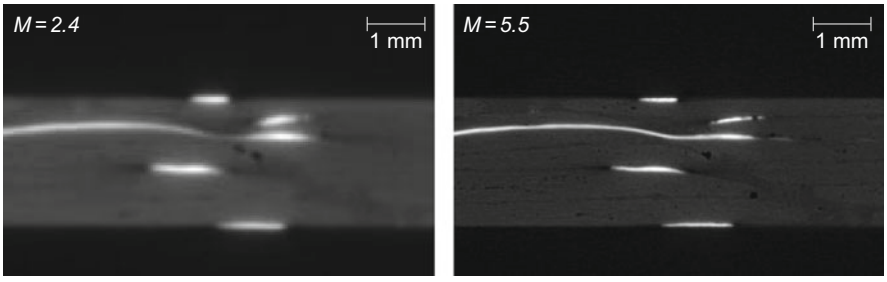

Fig. 6.5 Comparison of CT scan slice of same object with different magnification factors

The acquired digital images are spatially discretized by the pixel array of individual size $\widetilde{P}$. This constitutes the fundamental length scale of spatial resolution at the position of the detector. The absolute resolution of the volume produced from such 2D images is generally referred to as voxel size $\tilde{V}$, which is defined by the pixel size $\widetilde{P}$ and the geometric magnification factor M:

$$\widetilde{V} = \frac{\widetilde{P}}{M} \tag{6.2}$$

The overall resolution of the system is further limited by the effect of unsharpness resulting in blurred images. The geometric unsharpness d_g is mostly due to the focal spot size $\widetilde{F}$. The latter causes a penumbra effect as seen in Fig. 6.4b and may be written in terms of the geometric magnification as

$$d_g = \widetilde{F}(M-1) \tag{6.3}$$

Thus, the higher M, the larger the impact on d_g as seen by the schematically comparison in Fig. 6.6.

Finally, the mechanical stability of the configuration may result in unintended movement of the object and thus may introduce additional movement unsharpness d_{mov}. The latter is linked to the rotation of the test object and may be induced by tilting of the object during scanning. However, given the test object is tightly fixed and has sufficient stiffness, this effect is usually negligible. As another factor of mechanical movement during image acquisition, temperature gradients may cause a slow change in the dimensions of the test object or the geometric arrangement as such. Under usual operating conditions, the CT systems are designed in a way that the thermal expansion of the system is minimal and therefore the effect is usually also negligible. For the dimensional change of the test object, the thermal conductivity and the thermal expansion coefficients are relevant quantities. These strictly depend on the scanned material and thus may induce according thermal expansion of the test object. However, within the usual change of temperature, this effect is negligible for most materials. The sum of all of these movement effects will lead to

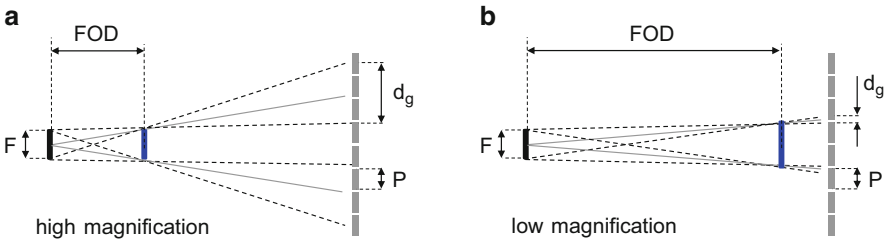

Fig. 6.6 Relation between magnification factor and geometrical unsharpness for high (**a**) and low (**b**) magnification factor

an additional unsharpness proportional to M in the acquired image and, hence, will directly influence the resolution of the volume.

The total unsharpness d_{tot} of the system may then be derived by combination of the geometric unsharpness, the movement unsharpness, and the pixel size, yielding

$$d_{\text{tot}} = \frac{1}{M}\sqrt{d_{\text{mov}}^2 + d_{\text{g}}^2 + \widetilde{P}^2} = \sqrt{\left(\frac{d_{\text{mov}}}{M}\right)^2 + \left(\frac{\widetilde{F}(M-1)}{M}\right)^2 + \widetilde{V}^2} \tag{6.4}$$

Thus for a detector pixel size $\widetilde{P} \ll d_{\text{tot}}$ and $d_{\text{mov}} \to 0$, the focal spot size is the limiting factor for image resolution. In contrast, for pixel size $\widetilde{P} \gg d_{\text{tot}}$ and $d_{\text{mov}} \to 0$, the pixel size will be the limiting factor.

In high-resolution imaging, the ultimate resolution is usually limited by the focal spot size $\widetilde{F}$. For the case of microstructure as found in fiber reinforced materials, an empirical value of the maximum detail detectability may be approximately 1/3 of the focal spot size $\widetilde{F}$.

As an example of this relationship, a series of cross-sectional images of the same object are shown as function of the focal spot size $\widetilde{F}$ in Fig. 6.7 for a constant magnification factor $M = 5.5$. Clearly, the smallest spot size comes with best detail visibility. When changing $\widetilde{F}$ to larger sizes, this induces noise in the images, therefore reducing the possibility to resolve details of the composite microstructure.

6.2.2 *Artifacts*

In the context of computed tomography, the term artifact is applied to any systematic discrepancy between the attenuation values in the reconstructed volume and the true attenuation coefficients of the test object [10, 11]. CT images are easily affected by various artifacts since the final volumetric image is based on a multitude of independent measurements. The reconstruction algorithm assumes that all these measurements are consistent, so any inconsistency during the measurement will directly transfer into an error in the reconstructed volume. As general terminology used for artifacts in computed tomography, Barrett and Keat suggest the following four artifact types [10]:

(a) Streaking
(b) Shading
(c) Rings
(d) Image distortion

Further it is possible to group the artifacts according to their origins into four categories:

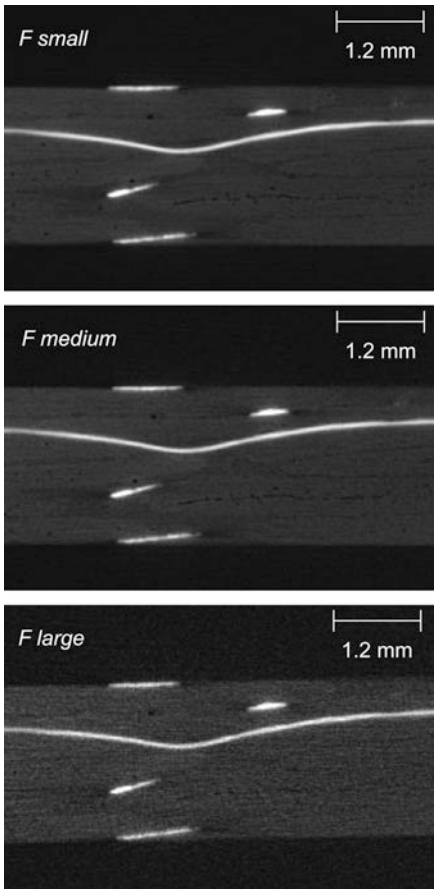

Fig. 6.7 Comparison of CT scan slice of same object with different spot sizes $\widetilde{F}$ at constant magnification factor $M = 5.5$

1. Physics-based artifacts, which result from the physical processes involved in the acquisition of the projection images
2. Hardware-based artifacts, which result from imperfections in the acquisition system
3. Reconstruction artifacts, which are caused by the deficiencies in the image reconstruction process
4. Motion artifacts, which are caused by movement of the test object during acquisition

In the following, typical artifacts of these four categories are discussed following the considerations made by [10] for medical applications, but are generalized in their meaning to the field of material analysis, and distinct examples in application to fiber reinforced materials are presented.

6.2.2.1 Physics-Based Artifacts

Beam Hardening

As a polychromatic X-ray beam passes through matter, low-energy photons are preferentially absorbed, and the attenuation is no longer a linear function of absorber thickness. Hence, the beam becomes "harder" because the lower-energy photons are absorbed more rapidly than the higher-energy photons, and therefore the mean energy of the beam increases [10, 12]. This may induce several types of artifacts frequently occurring during scans of fiber reinforced materials. Among the types of beam hardening artifacts, there are the so-called cupping artifacts, the appearance of dark bands or streaks between objects with high density, and the glooming of high-density inclusions. Several algorithms are available in modern reconstruction programs to minimize the effect of beam hardening to some extent [13–15].

Cupping Artifact

The occurrence of cupping artifacts is readily explained following [12] by considering the attenuation profile observed for a uniform cylinder as seen in Fig. 6.8a. Ideally, the attenuation profile would resemble a certain shape allowing a reconstruction of the cylinder in its expected shape. However, the beams passing through the center of the cylinder suffer more from beam hardening than those passing the edges. Since higher-energy X-rays are attenuated less during propagation, the projection areas with more beam hardening suffer less from attenuation than theoretically expected. The reconstruction of these falsified projections thus causes a characteristic cupped shape at the edges of the cylinder.

This type of artifact is frequently observed at the edge of the material, i.e., the interface between the surrounding air and the solid. This causes the white shade at the edge of the cross-section of the fiber reinforced material seen in Fig. 6.8b and should not be misinterpreted as material with higher density.

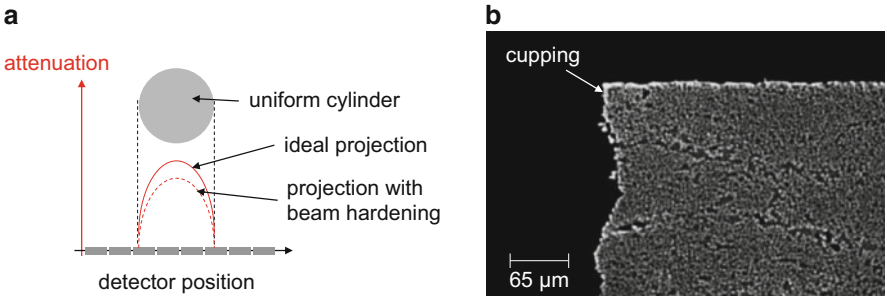

Fig. 6.8 Attenuation profiles obtained with and without beam hardening for an X-ray beam passing through a uniform cylinder (**a**) and example of cupping artifact in CT scan (**b**)

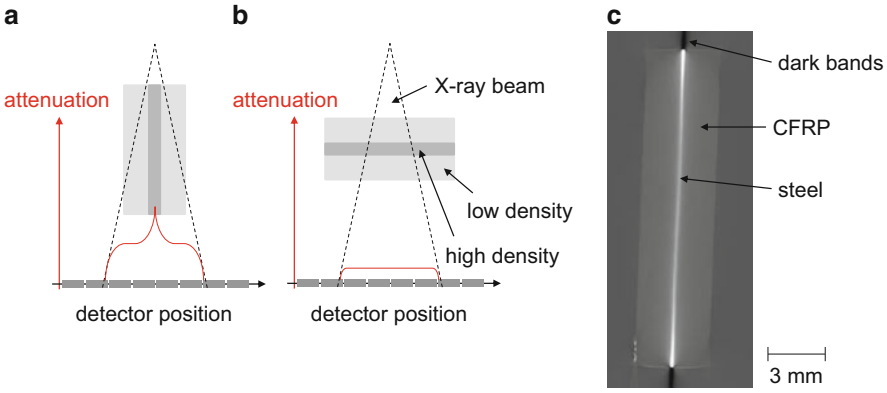

Fig. 6.9 Origin of dark bands due to beam hardening effects (**a**, **b**) and example of dark bands due to high-density inclusion (steel layer) in a carbon fiber reinforced polymer (**c**)

Dark Bands

Another type of artifact, which may occur due to beam hardening, are dark bands caused by spatially close high-density inclusions or oriented high-density materials. In such a situation, the incident beam is affected more by beam hardening for the path between source and detector where the high-density object is aligned with the beam direction (Fig. 6.9a) and suffers less for the path perpendicular to this arrangement (Fig. 6.9b). As consequence, the regions behind projection directions with strong beam hardening appear with higher density than in reality. This effect is visible as dark bands extruding from these projection directions. As an example for this effect, a reconstructed slice of a CT scan of a fiber-metal laminate is shown in Fig. 6.9c. In this case, the thin steel layer has much higher density than the surrounding fiber reinforced material and therefore acts as high-density inclusion. Along the long axis of the metal sheet, strong dark bands extrude from the position of the specimen edge.

High-Density Foreign Material Artifact

Similar to the previous two effects, the presence of a material with comparatively high density to the surrounding material can generally lead to visible streaking artifacts. These typically occur because the density of the material may exceed the measurement range of the detector system and thus results in an incorrect attenuation measurement. In the context of fiber reinforced materials, any metallic inclusions may cause this type of artifact. Since metallic materials attenuate the X-ray beam much more than the polymeric matrix system or the typical reinforcement fibers, the attenuation values of objects behind the metallic inclusion are measured too high. Due to the application of the reconstruction algorithm to this

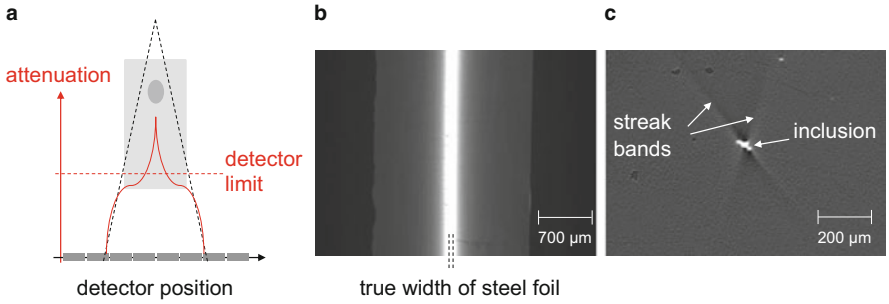

Fig. 6.10 Wrong measurement of attenuation profile due to detector limit (**a**) and example of gloom due to high-density inclusion (steel layer) in a carbon fiber reinforced polymer (**b**) and example of streak bands due to high-density particle inclusion in a carbon fiber reinforced polymer (**c**)

incorrect measurement of the attenuation profile, bright and dark streaks in transverse directions to the rotation axis may appear in the CT image.

The effect of this incorrect measurement of the density is visible as bright glow around the high-density object. For the case of the fiber-metal laminate shown in Fig. 6.10b, this causes a characteristic glow at the interface between the thin metallic sheet and the fiber reinforced material reducing visibility of details at this interface. As another example, streak bands due to a particle of high density included in a fiber reinforced polymer are shown in Fig. 6.10c.

Partial Volume Averaging

The algorithms used in CT data reconstruction assume that the object is completely covered by the detector at all view angles and that the attenuation is caused by the object only. In cases where this situation is not fulfilled, the CT reconstruction starts to show truncated sections. Due to the divergence of the X-ray beam, this is usually visible at the end of the reconstructed volume if the scanned region is smaller than the object (see Fig. 6.11a). This occurs because the finite size of the detector does not allow measuring the full attenuation profile of the cone beam, since the red areas are not equally scanned at all angles. This effect is exemplarily shown for a reconstruction of a piece of fiber reinforced material in Fig. 6.11b.

Another artifact related to the partial volume effect is mostly relevant to the specific scanning configuration of helix tomography. Here line scanners instead of array scanners are used to produce each reconstructed slice. The feed of the test object is done mechanically, so the thickness of each slice is determined by the feeding speed. Considering the scheme in Fig. 6.12, the challenge is to provide an equal lateral resolution along all three axes for reconstructing the volume image. If the slice thickness is chosen large compared to the lateral size of the pixel, its aspect ratio gets distorted and the contained information is smeared out (cf. Fig. 6.12a). Here the length of the voxel along the feed axis is much larger than in the directions

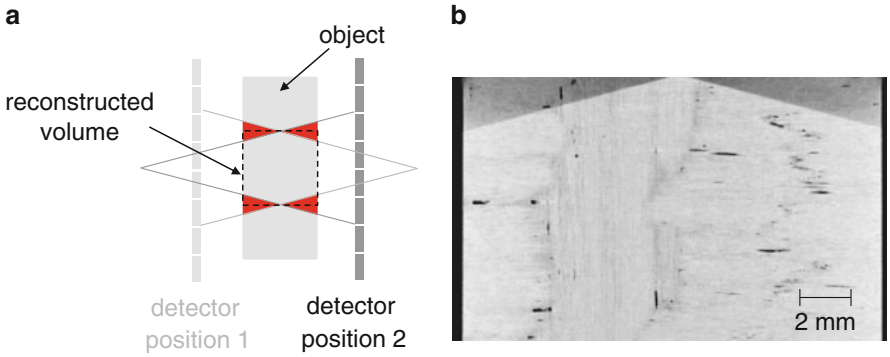

Fig. 6.11 Scan configuration (**a**) and example of partial volume effect upon reconstruction (**b**)

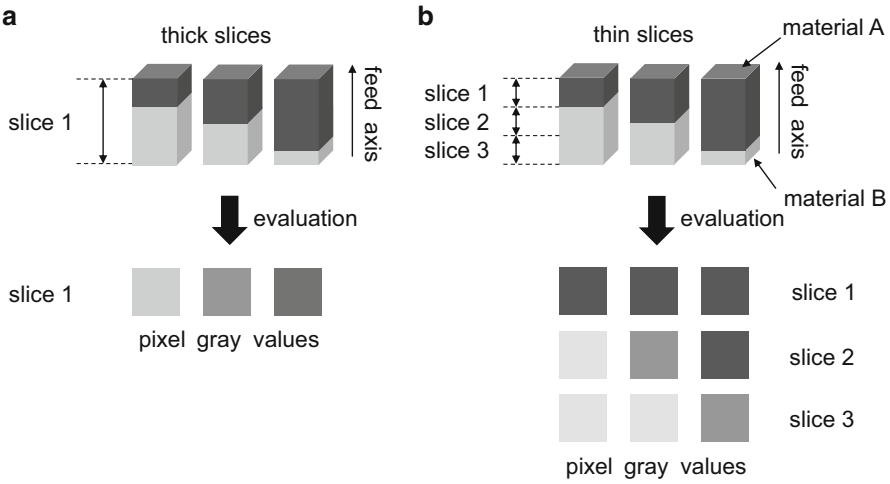

Fig. 6.12 Origin of spillover effect and distortion of voxel aspect ratio causing blurred information in the feed direction due to thick slices (**a**) compared to thin slices (**b**)

perpendicular. This averaging effect is called spillover and manifests itself in a blurred image information along the direction of object feed. Selecting thin slices instead allows keeping a decent aspect ratio of the voxel and retains sharp gradients of material density (cf. Fig. 6.12b).

Quantum Mottle (Noise)

Another trivial type of artifact is due to quantum mottle. The origin of this effect is the incident background radiation seen at the detector, which superimposes to the scan beam. This results in a grain noise structure seen on the image and thus

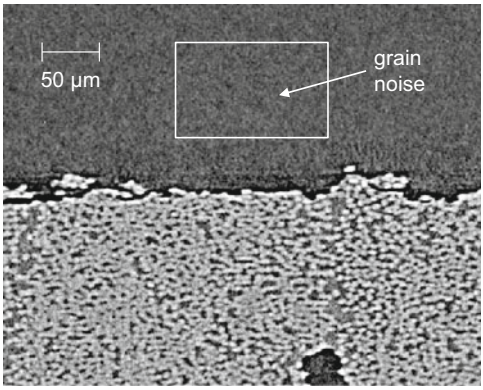

Fig. 6.13 Example of grain noise in CT image

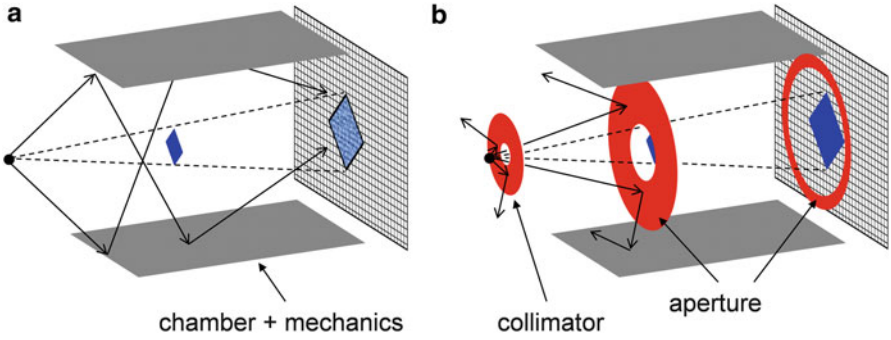

Fig. 6.14 Scheme of measurement configuration without (**a**) and with (**b**) additional collimator and apertures to reduce the intensity of secondary X-rays incident to the detector

resembles an artificial scatter of density. This noise is composed of the general cosmic background noise and the secondary reflections of the X-ray beam, which are incident to the detector at other angles than through the test object. As seen in Fig. 6.13, this is typically pronounced for scans with a low signal-to-noise ratio. The latter may occur for setups with X-rays barely able to penetrate the test object due to its thickness or absorption, but also when attempting to distinguish materials with close-by density such as carbon fibers and polymer matrix systems (see Fig. 6.13).

Some X-ray CT devices use additional shielding measures to reduce the amount of secondary X-ray photons to the detector. In this context "secondary" refers to any backscatter produced by interaction of the primary X-ray beam with other pieces of the equipment, such as the shielding cabinet or the included mechanics. In the configuration shown in Fig. 6.14b, the presence of apertures collimates the primary beam and shields the cabinet from the incident X-rays so the amount of secondary X-rays gets substantially reduced.

Photon Starvation

Another potential source of streaking artifacts is photon starvation. This may occur for objects with highly attenuating areas in some of the projection directions. Similar to the dark bands, these are caused by the relative alignment of the test object and the source-detector axis. Other than for beam hardening the present effect is due to a lack of photons arriving at the detector in general, rather than a falsified attenuation profile. Therefore some of the orientations suffer from noisy projection images. The consequences are streaks in the reconstruction plane, i.e., perpendicular to the rotation axis. For scanning of materials, this effect may be avoided by previously selecting the orientation with highest attenuation and suitably adjusting the X-ray intensity to avoid photon starvation at these angles. However, for geometries with strongly distorted *x*/*y* aspect ratio, this may come with the cost of saturating the X-ray detector at the other projection angles, so suitable trade-off might be required.

Undersampling

As a fundamental principle to computed tomography, the number of projections should be sufficient to allow a reasonable reconstruction of the specimen volume. If the number of projections gets too low (undersampling), the first artifact to observe is ray aliasing at sharp edges and at narrow details. This is seen for the object in Fig. 6.15 being visible as discrete stripes at some distance to the scanned object.

If the overall number of projections gets even lower, severe imperfections of the scanned object can be expected. This is seen in Fig. 6.16 for a decreasing number of projection images as basis for the same reconstruction algorithm. For the full set of 736 images, the rectangular cross-section is well reconstructed, but also the occurrence of dark bands is seen as extension to the longer axis edges of the material. With reduced number of images, the rectangular cross-section is hard to be reconstructed accurately, and an increasing amount of ray aliases occur.

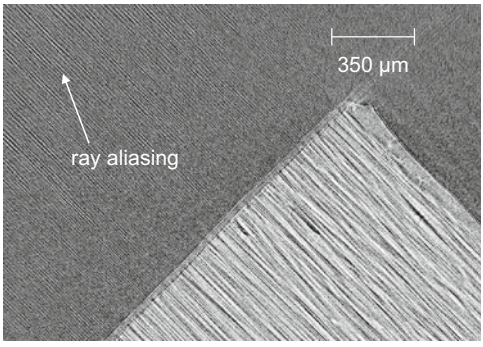

Fig. 6.15 Example of ray aliasing due to undersampling

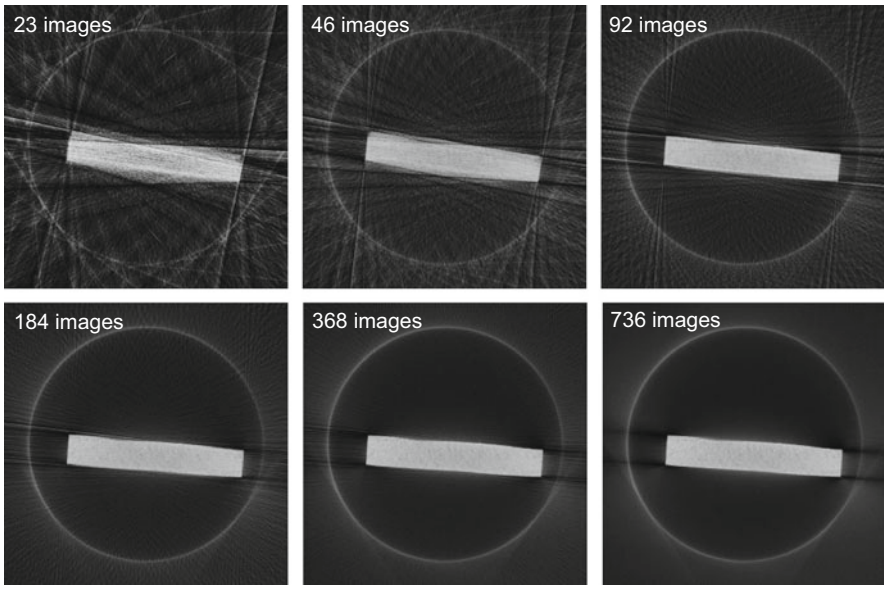

Fig. 6.16 Example of image reconstructed with different numbers of projections

6.2.2.2 Hardware-Based Artifacts

Ring Artifact

The ring artifact is probably the most common hardware-based artifact. It appears as image of one or more "rings" within the reconstruction plane. If one of the pixels of the detector is corrupted or badly calibrated, the detector will give a consistently false reading at each angular position. During the reconstruction process, this turns into a circular artifact with the circle extension being perpendicular to the rotation axis as seen in Fig. 6.17. The appearance of such ring artifacts naturally lowers the image quality, since it tends to overlap with parts of the image reducing the visibility of details in these areas. Modern CT systems allow recalibrating the detector system to reduce the occurrence of ring artifacts by simply removing the information of dead pixels in the detector unit. Similarly, some reconstruction algorithms explicitly focus on suppression of ring artifacts by removing the dead pixel content during the reconstruction process.

Tube Arcing

During operation of X-ray tubes, the occurrence of short circuits within the tube may cause image artifacts due to tube arcing. The electrical shortcut typically emanates from a spark between the cathode and tube cover, which causes a spontaneous loss of X-ray intensity. The occurrence of this effect is linked to the tube design and the particular reliability of the individual tubes.

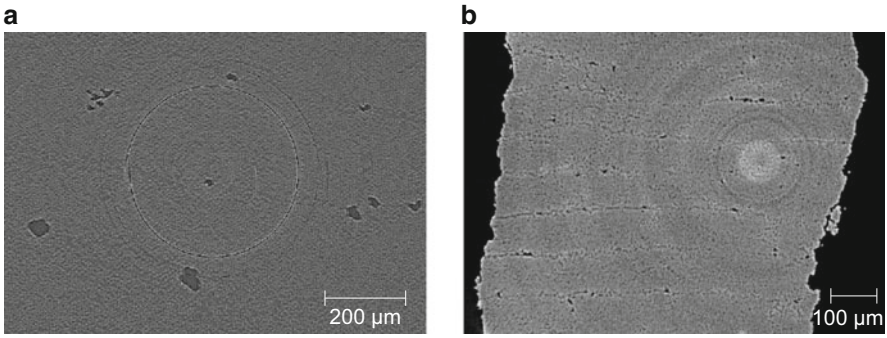

Fig. 6.17 Examples of ring artifacts due to dead pixel (**a**) and due to bad calibration range (**b**)

6.2.2.3 Reconstruction Artifacts

The next class of artifacts arises from the (physical) imperfection of the incident X-ray beams and the according assumptions made in the reconstruction process. Since this is different for the configurations of cone-beam CT and helical CT, the resulting types of artifacts are distinguished based on these two arrangements in the following.

Cone-Beam Effect

For the cone-beam CT configurations, further distinction is made between line-scan detectors resulting in fan-shaped beam geometries and the array detectors resulting in a cone-beam shape of the X-ray beam (cf. Fig. 6.18). Due to the physical size of the beam geometries, the collimators can be closed more for the line scanners but need to stay open more for the array detectors. As a consequence of the cone-beam geometry, the photons collected at the detector position do not only originate from the ideal transmission path along an ideally flat plane configuration achieved in the fan-shape geometry but are also incident at other angles. This effect becomes more pronounced the farther away the scan object is from the ideal rotation axis. Thus to minimize the effect, it is most suitable to position the test object at the center of the rotation axis. However, modern CT systems are readily equipped with cone-beam reconstruction algorithms, so this effect does not play an important role in such systems anymore.

Windmill Artifacts

The windmill artifacts are linked to the use of helical CT device for the scan. The two most well-known artifacts for these systems are the zebra artifact and the stair-step artifact. As zebra artifact, a periodic modulation of light stripes parallel to the

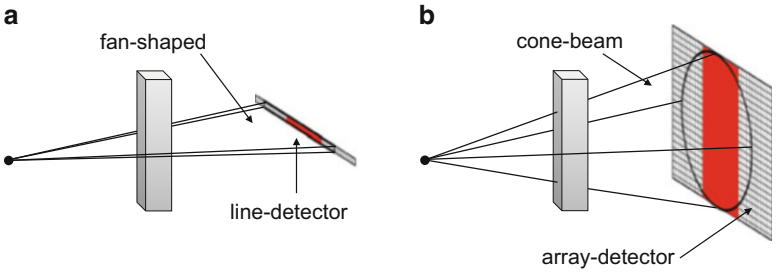

Fig. 6.18 Difference between line-scan arrangement (**a**) and array detectors (**b**)

axis of rotation may appear in the images, which is due to the helical interpolation process causing a modulation of the noise level. This effect starts to be more pronounced at some distance to the axis of rotation. As a stair-step artifact, the misalignment of the individual slices during stacking along the axis of rotation is known. This causes steplike contours responsible for the name of this artifact.

6.2.2.4 Motion Artifacts

Motion artifacts may result from sudden movement or relaxation of a test specimen being scanned. This results in unequal projections of the angles before and after movement and therefore needs to be avoided for proper reconstruction of the volume. For most of the CT scans involving fiber reinforced materials, motion artifacts may not seem to be of huge relevance. If the specimen is tightly fixed to the rotary table, there is no strong likelihood of sudden movement of the specimen. From medical imaging, the consequence of such sudden movement in CT imaging is well known, and motion artifacts usually appear as shading or streaks in the volumetric image or may even render the whole scan useless if the movement was too high.

However, for the in situ load stages discussed herein, there is a certain likelihood of motion artifacts during scanning. For the test object being scanned still subject to mechanical load, the occurrence of partial failure during the acquisition process may cause small movements of the scan object and thus cause the aforementioned artifacts. This is exemplarily seen in the example of a fiber reinforced material recorded within a tensile load stage as seen in Fig. 6.19. While the bottom part of the CT scan is free of motion artifacts, the upper half of the fractured material was subject to sudden secondary failure causing an additional motion during the acquisition procedure turning into the blurred representation seen best at the edges.

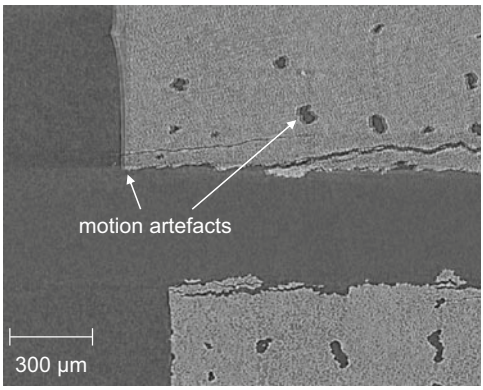

Fig. 6.19 Motion artifact in upper half of fractured material as observed in in situ load stage

6.2.3 Detectability of Defects in Fiber Reinforced Materials

High-resolution computed tomography can be used to identify microstructures in composite materials, such as fiber distributions [16–18], void volume fractions [19–24], and damage mechanisms such as cracks and fiber breaks [25–34] occurring within the volume of the material. A high level of confidence can be placed in the results as the features are viewed directly at the relevant length scale. In the following some representative examples of computed tomography images of fiber reinforced materials are presented to demonstrate the current capabilities of high-resolution computed tomography devices in application to fiber reinforced materials. Such high-resolution X-ray CT has gained considerable interest as a powerful tool for material studies directed to understand interaction of composite failure mechanisms [31, 35, 36]. Advances in the last decade now provide established 3D imaging routines in the micrometer and sub-micrometer range. This method is gaining importance in engineering and material science to determine the internal characteristics of materials and their behavior [37]. In the case of fiber reinforced materials, CT has been used to identify material characteristics like fiber orientation and volume fraction at the sub-ply level, and failure mechanisms, such as ply cracks [31, 32, 34, 38] and fiber failure [39, 40]. Among the multitude of possibilities, a particular focus is given to the detectability of damage mechanisms in the following, since this is the main topic within this book.

Figure 6.20a–d shows CT results of a fiber reinforced laminate with $[(0/90)_2]_{sym}$ stacking sequence made from a Sigrafil CE1250-230-39 prepreg. The 17 mm × 150 mm × 2.2 mm specimen was first subject to tensile load according to DIN-EN-ISO 527-4 to induce some failure and was unloaded prior to ultimate failure, unmounted and scanned without further preparation. The according acquisition parameters of the scan are summarized in Table 6.1.

As seen in Fig. 6.20, the individual layers can clearly be distinguished based on their different fiber orientations. Also, a high level of detail can be observed for the inter-fiber cracks and inter-ply delamination present in the laminate. The details in Fig. 6.20b, c allow to spot inter-fiber failure in the 90° plies, inter-ply delamination,

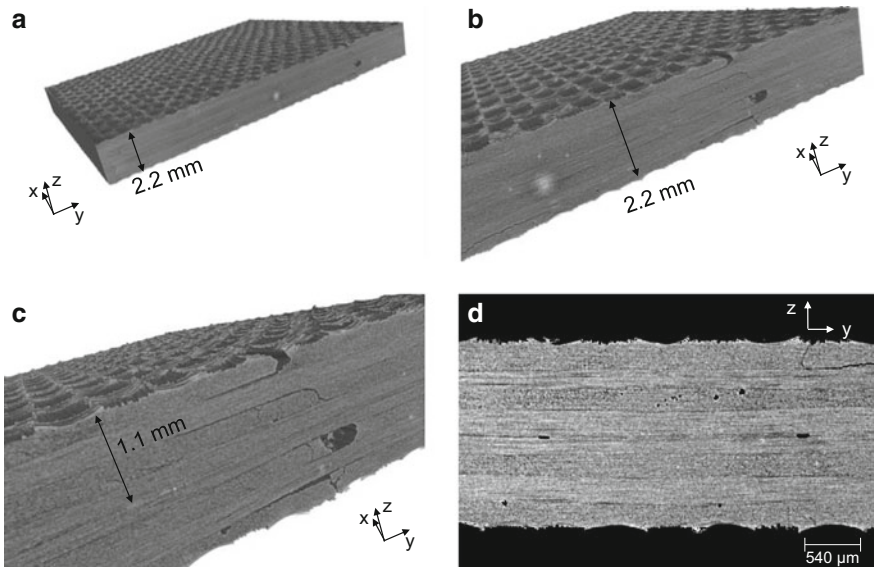

Fig. 6.20 3D representation of $[(0/90)_2]_{sym}$ laminate (**a**) and magnifications allowing to spot inter-fiber failure and inter-ply delamination in 3D volume according (**b**, **c**) and respective virtual cross-section (**d**)

Table 6.1 Acquisition parameters for scan of tensile specimens

Measurement parameter	Value
Detector type	Amorphous Silicon CsI detector $(3072 \times 2400)px^2$
Filter	None
X-ray tube voltage	90 kV
X-ray tube current	150 µA
Focal spot size	1.5 µm
Voxel size	7.8 µm
Acquisition angles	2000
Image exposure time	1.0 s
3D reconstruction software	Phoenix datos|x2 reconstruction

and inclusions like voids. Clearly one key advantage beyond classical microscopy investigations is the possibility to produce virtual cross-sections at arbitrary positions of the scanned volume. In contrast, optical and electron microscopy may offer even higher spatial resolution, but can only be carried out at surfaces, requiring either a preparation step after loading (losing any relation to the applied load or damage evolution) or via in situ analysis under a nonrepresentative stress state (i.e., monitored at free surface as opposed to the state within the bulk material). Polishing and cutting techniques commonly required for cross-sectional imaging can also induce artifacts which may be mistaken for features of interest.

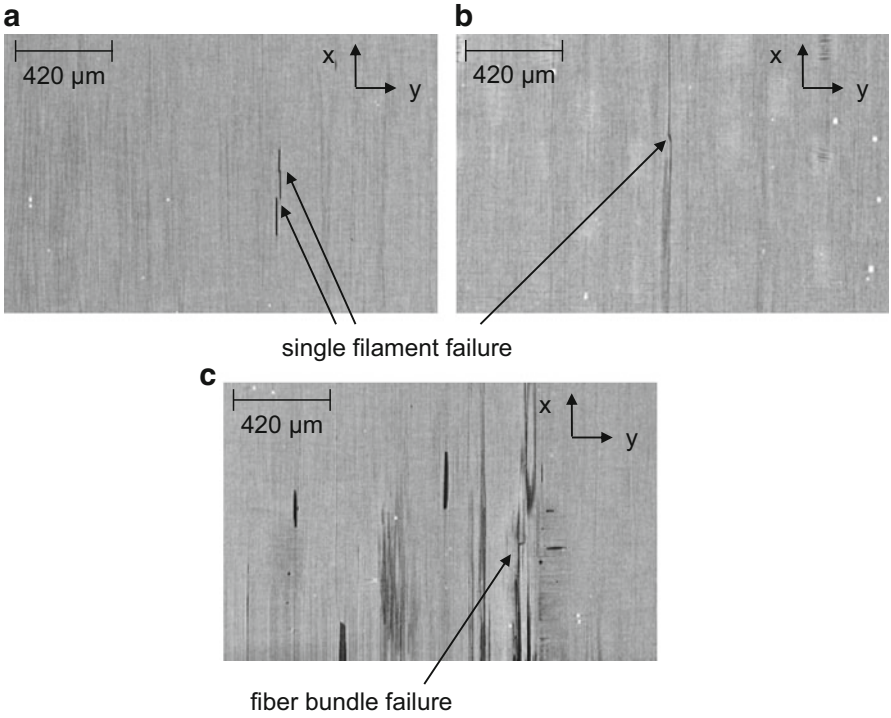

Fig. 6.21 Visibility of single carbon fiber filament failure (**a**, **b**) and fiber bundle failure (**c**) in 2D cross-sections of $[(0/90)_2]_{sym}$ laminate

Using a cross-section in the *xy*-plane, this allows inspecting the 0° layers for the occurrence of fiber breakage. As seen from Fig. 6.21a, b, the occurrence of single carbon filament failure (typical diameter 7 µm) is clearly visible from the cross-sectional images. Moreover, the initiation of matrix cracks at these positions causing splitting of the laminate in parallel to the fiber axis is also readily observed. In addition, Fig. 6.21c shows an example of a fiber bundle failure.

Another advantage of CT is to segment the scanned volume to retrieve only a particular part of the specimen. As seen in the 3D visualization in Fig. 6.22, this allows to artificially remove one part of a fractured body to reveal the internal fracture surface in a unidirectional T800/913 prepreg laminate. The high-resolution scan settings reported in Table 6.2 allow spotting a high level of detail at the fracture surface, such as the morphology and broken fiber filaments.

Using similar high-resolution settings reported in Table 6.3, CT scans also allow removal of the matrix material based on its density and to spot the remaining single carbon fiber filaments (cf. Fig. 6.23). This can be used to evaluate their orientation, to quantify their distribution, or to spot fiber filament breaks as seen in the lower left corner of the present HTA fiber bundle in a polyurethane resin. However, these

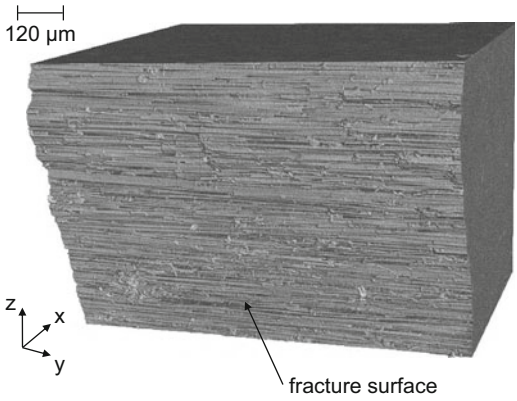

Fig. 6.22 Visibility of details on fracture surface of fiber reinforced polymer in high-resolution scan

Table 6.2 Acquisition parameters for scan of fracture surface

Measurement parameter	Value
Detector type	Amorphous Silicon CsI detector $(3072 \times 2400)px^2$
Filter	None
X-ray tube voltage	50 kV
X-ray tube current	170 µA
Focal spot size	1.1 µm
Voxel size	3.4 µm
Acquisition angles	1000
Image exposure time	1.5 s
3D reconstruction software	Phoenix datos|x2 reconstruction

Table 6.3 Acquisition parameters for high-resolution scan

Measurement parameter	Value
Detector type	Amorphous Silicon CsI detector $(3072 \times 2400)px^2$
Filter	None
X-ray tube voltage	70 kV
X-ray tube current	220 µA
Focal spot size	0.6 µm
Voxel size	0.7 µm
Acquisition angles	1800
Image exposure time	2.0 s
3D reconstruction software	Phoenix datos|x2 reconstruction

high-resolution images are only possible for specimen sizes small enough to permit short focus-object distances.

In particular for fiber reinforced materials, the damage zone is sometimes geometrically complex, and severe fragmentation during fracture is happening frequently. Thus conventional cross-sectioning techniques using resin embedding

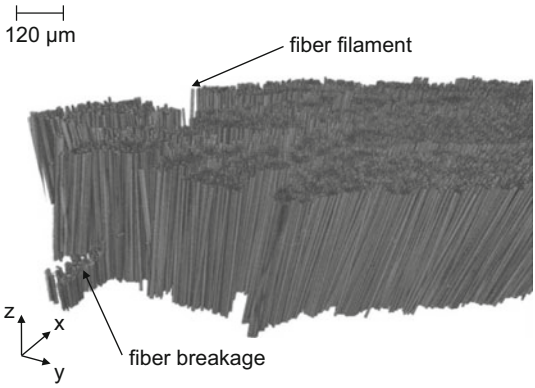

Fig. 6.23 Visibility of single carbon fiber filaments and fiber failure in 3D volume

Table 6.4 Acquisition parameters for scan of impact damage

Measurement parameter	Value
Detector type	Amorphous Silicon CsI detector $(3072 \times 2400)px^2$
Filter	None
X-ray tube voltage	50 kV
X-ray tube current	200 µA
Focal spot size	1.5 µm
Voxel size	27.5 µm
Acquisition angles	1000
Image exposure time	1.5 s
3D reconstruction software	Phoenix datos|x2 reconstruction

and mechanical grinding and polishing are somewhat limited as many of the small fragments are not conserved by this approach. Using a CT scan for such damage zones, these small details can readily be visualized. As seen for the example of impact damage in a carbon fiber/epoxy laminate with glass fiber rovings in Fig. 6.24, all small fiber filaments residues and epoxy resin fragments can be spotted, and the geometrical complexity is much better represented in a 3D image than in a simple 2D cross-section.

The analysis of porosity inside a laminate has achieved high attention within the last decade [19–24]. Due to the direct visibility of gaseous inclusions within the laminate, the direct quantification of their volumetric fraction is tempting, but standardized procedures are still subject to recent research efforts. As an example of the visibility of voids on the micro- and mesoscale, two examples are shown in Fig. 6.25a, b for a CT scan with the parameter settings of Table 6.1. Extensive studies have been carried out to investigate the visibility and accuracy of void dimensions as function of CT scan parameters [21, 23, 24]. Since the quantification of such inclusions is not within the scope of this book, this aspect will not be

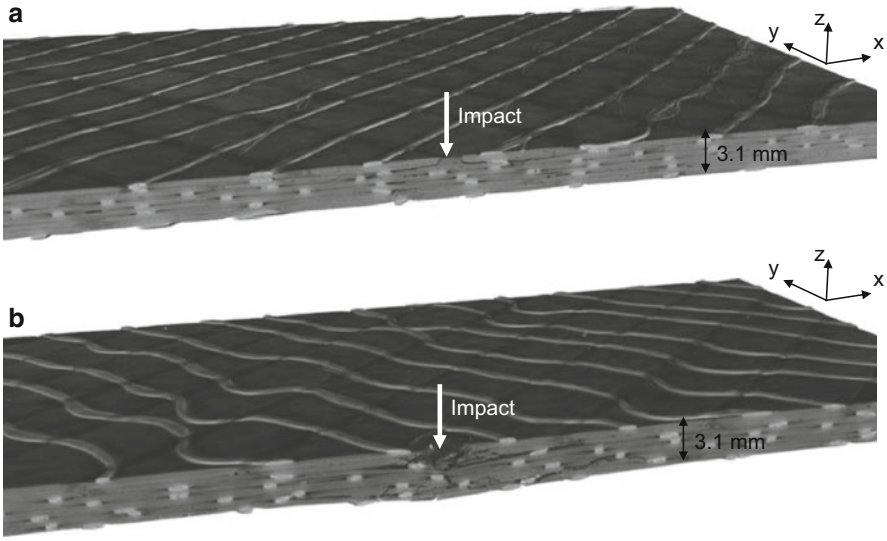

Fig. 6.24 Scan of damage zone as due to impact damage in 3D view for low- (**a**) and high-energy impact (**b**)

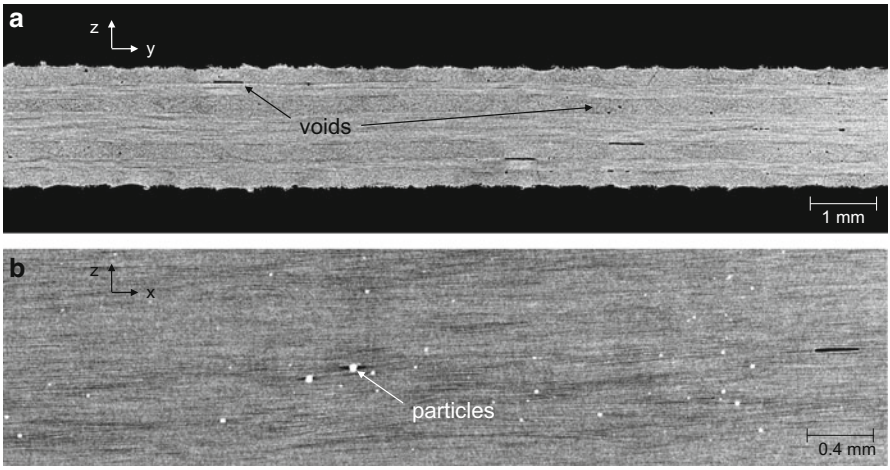

Fig. 6.25 Detectability of voids and foreign material inclusion in $[0/90/0/90]_{sym}$ laminate

covered in the following. Also visible in Fig. 6.25b are examples of foreign material inclusions identified as bright particles. Such inclusions may result from impurities during the production process, but may also be part of the resin systems, i.e., as flame retardants.

6.3 Volumetric Inspection of Materials

As demonstrated within the previous sections of this chapter, computed tomography provides a microscopy method suitable to visualize the interior structure of a fiber reinforced composite. Still the approaches presented so far are merely a substitute to other microscopy techniques. In the following, distinction is thus made between concepts used for ex situ loading, removal of the specimen, and subsequent scanning in contrast to approaches using in situ loading of materials and subsequent scanning.

6.3.1 Concepts for Ex Situ Loading

The basic concept for ex situ loading is a straightforward combination of a test rig as conventionally used for mechanical loading of a material and a CT scanner. As schematically shown in Fig. 6.26, the specimen is first loaded within the test rig until a certain damage state is reached. The relevance of the load level for inspection may either be based on signatures in stress-strain curves or based on secondary methods such as acoustic emission. The next step consists of dismounting the specimen and taking to the CT device. Subsequently a CT scan is made and the specimen is potentially remounted in the mechanical load rig to increase the mechanical load level. To this end a sequence of damage states may be recorded

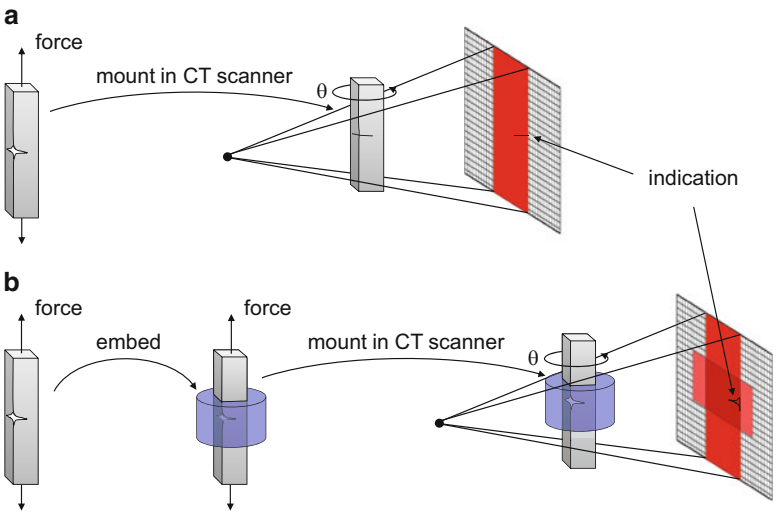

Fig. 6.26 Scheme of ex situ loading in combination with CT scan (**a**) and by using potting material to embed damage zone (**b**)

as discrete volumetric images to allow assessment of the present damage status of the specimen [29, 41–45].

However, the release of the applied mechanical load during dismounting may cause a closure of small cracks and, therefore, render them invisible during the CT inspection. Hence it might be necessary to preserve the stress-strain state within the material during scanning. To this end an approach using epoxy resin as potting material to embed the specimen under load can be applied [44]. Typically fast-curing epoxy resins without high-density fillers are used to avoid generation of artifacts within the epoxy resin. Optical transparence is not of vital importance since the X-rays will penetrate the material, but it helps to later select the correct portion of the specimen for a precise cutting process. For the purpose of segmentation and to increase visibility of the specimen, a noticeable difference in material density between the potting material and the embedded fiber reinforced polymer is recommended. This may be subject to trial and error, since typically the difference in density values is very low, when comparing values of epoxy resins used as potting material and values of the epoxy resins used as matrix materials. Ultimately, this procedure will assure that a certain portion of the original stress-strain state is preserved within the specimen, and small cracks will be better visible. As disadvantage, the specimen cannot be remounted to the test rig for further loading, and there is some justified doubt, whether this procedure fully inhibits specimen relaxation. Therefore any quantitative information like separation of crack walls or other geometric measurements need to be taken with necessary care. Also, from a practical point of view, some initial experience is required to perform the potting process within a mechanical test rig since the relevant portion of the specimen usually is in the middle of free air or barely accessible due to the load fixtures. In practice this means that suitable potting compounds need to be fabricated for each specimen type. Moreover, with the specimen being under load during this procedure, according safety measures are required to avoid unintended failure during a hold cycle.

6.3.2 Concepts for In Situ Loading

In order to perform in situ observations of material failure, further modifications to the established test setups are required. As major difference to the ex situ approach, the configurations discussed in this section use an arrangement as shown in Fig. 6.27. Here, the load rig is mounted in situ within the CT scanning device [25, 26, 31, 34, 35, 40, 46–61]. For the implementation of these concepts, three experimental factors may be distinguished and shall be discussed in the following. These are the type of X-ray source, the type of X-ray detector, and the type of load rig.

As general remark to all of the techniques mentioned within this section, it is important to understand that none of these CT techniques really operates in a real-time sense. Although comparatively fast scans are possible nowadays and the

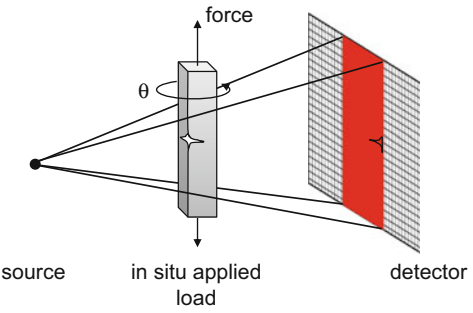

Fig. 6.27 Experimental configuration for in situ loading during CT scan

reconstruction time may be of similar order, the specimen still is required to be kept under a certain load for durations of minutes to hours during scan operation. This will allow stress relaxation within the material and therefore will alter the "true" geometry of the specimen. Hence all practical implementations make use of a short duration to allow for stress relaxation of the specimen before scan operation in order to avoid motion artifacts. Therefore, the name in situ is only considered to be correct in the sense that the specimen does not need to be dismounted from an external load rig to be inspected by CT. Nevertheless, this approach enables several new possibilities for analysis of failure behavior of fiber reinforced materials, so it is worthwhile to consider some of the technical details of this approach more precisely.

6.3.2.1 Type of X-ray Source

The majority of the published approaches were carried out using synchrotron-based CT scanners in conjunction with specifically developed load rigs [25–28, 31, 32, 34–36, 38, 40, 42, 45, 46, 49, 57, 61–64]. The main reason for this trend is the high brilliance and high intensity of the synchrotron beams in combination with a small spot size assuring high-resolution imaging as discussed in Sect. 6.1. Since commercial devices hardly could compete with any of these three aspects, only few attempts have been made to use commercial CT scanners for in situ inspection with a level of detail as discussed in Sect. 6.2. Nowadays there are some first CT scanners which provide voxel resolutions in the sub-micrometer range and are thus suitable to resolve the microstructure of a fiber reinforced polymer. One of the key arguments in favor for commercial X-ray CT scanners is without doubt the price and the availability. However, the intensity of commercial X-ray tubes is hardly comparable with the photon flux reached at typical synchrotron beam lines, so the contrast resolution is still not within the same range, and scan durations are typically much longer. Since longer scan times increase the chance of motion

artifacts and may also induce motion unsharpness, these should be kept at a minimum. Therefore, a suitable trade-off between the necessary detail visibility[2] and the scan duration is required.

6.3.2.2 Type of X-ray Detector

Similar to the X-ray source, the type of X-ray detector is of relevance when considering in situ inspection of materials. Because both devices are usually coupled to form one scanning device, it is not straightforward to discuss them independently, but since a variety of configurations is encountered in practice, the relevant parameters of the detector system shall also be briefly discussed. Regardless of the X-ray source, one can distinguish between line detector and array detector systems as previously discussed in Sect. 6.2. The key advantage of line scanners in the present context is their fast scan times as compared to array detectors. If the in situ inspection is restricted to a particular cross-section within the material (cf. Fig. 6.28a), this enables very fast scan times even with typical commercial X-ray sources. Here typical scan durations were found to be in the order of few minutes and thus reducing the likelihood of motion artifacts. Obviously, the drawback of this detector configuration is the lack of 3D information of the material interior. So unless damage is expected to occur at a distinct position (i.e., at a notch) or is expected to be randomly distributed, it is very likely to miss damage formation in some parts of the specimen under load. Hence, to retrieve information out of a certain volume of the material, either subsequent line scanning or an inspection using an array detector system is the only choice (see Fig. 6.28b). For all other technical aspects of the detector system, the same considerations as for conventional X-ray CT scans apply.

6.3.2.3 Type of Load Rig

As key component of the in situ loading concept, the load rig is discussed next. From the mechanical engineering perspective, one challenge is to apply a certain stress on the test specimen, while being able to rotate the whole configuration ideally by 360° without having any additional obstacles within the projection area. Since any applied load also needs to be compensated within the rig, the typical scheme of a load test rig is of composed of the components shown in Fig. 6.29. These comprise the specimen fixtures, a stationary (fixed) part and a moving part driven by an actuator imposing a displacement to the specimen. In typical laboratory size machines, the vertical glides are simple columns, and the stationary and

[2] As the first approximation, an increase of the number of projections and an increase of the exposure time can be assumed to be beneficial for detail visibility if low photon intensity is given. Both parameters add to the overall scan duration.

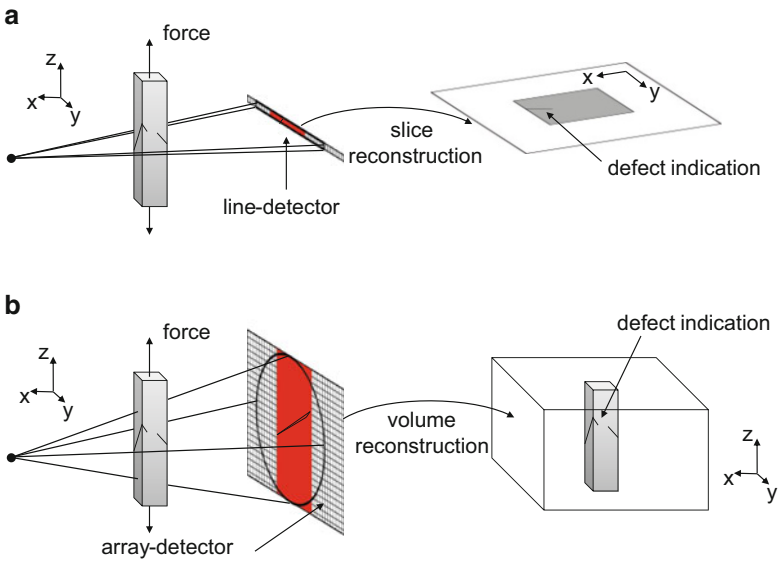

Fig. 6.28 Defect indication as retrieved from in situ measurement using line detector (**a**) and using array detector (**b**)

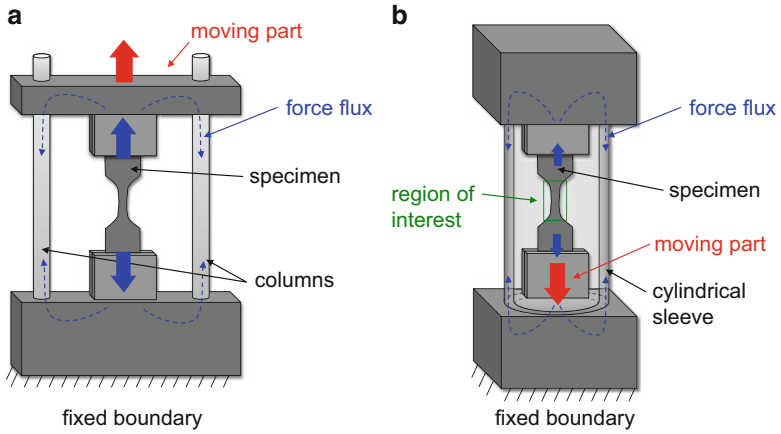

Fig. 6.29 Scheme of conventional load test rig using columns (**a**) and load test rig using cylindrical sleeve for load deflection (**b**)

movable parts of the machine are simple beams. If the whole configuration now is rotated around its center axis, it will be subject to substantial artifacts caused by the presence of the columns when passing the projection area. Hence, a configuration using a radially symmetric geometry as shown in Fig. 6.29b is favored from this perspective. Moreover, having the bottom fixture as moving part also enables a simple mechanical design for the upper part of the test rig. Thus the upper part is

chosen as stationary fixture, and the lower part is fully instrumented by an actuator and a load cell. The force flux for both cases is indicated by blue dashed arrows.

In order to ensure high detail visibility, further considerations with respect to the material used for the load rig are required. Since metallic parts exhibit comparatively high X-ray attenuation, a presence of these parts within the projection area should be avoided as much as possible. To scan the region of interest shown in Fig. 6.29b, materials with low X-ray attenuation should be applied at all positions within the projection path. Nevertheless, these parts are meant to carry the full mechanical load as applied to the specimen, so they need to be of a sufficient cross-section to avoid buckling or failure of the load rig. Here polymer materials are among the first choices when designing this part of the load rig, which is typically done in the shape of a tube. Transparent polymers are technically not required since the X-rays will penetrate the polymer material, but they allow for visual inspection of the specimen alignment and also were found to improve the handling during mounting of specimen. To select a transparent polymer, further aspects may also be considered. First, the material should be able to withstand X-ray intensity for an extended period without optical or mechanical degradation. Second, the microstructure of the material should be homogeneous and free of textures, which could cause artifacts reducing the detail visibility of the scanned specimen.

In order to achieve highest possible resolution, the limiting factor in terms of the described configuration is the distance between the center of the test specimen and the outer dimension of the test rig. Hence, this value should be minimized to achieve high-resolution images. Due to the combination of the aforementioned aspects, the load deflection concept using a tube (cylindrical sleeve) instead of columns is generally favored, since this geometry is fairly stable to withstand buckling and comes with a larger effective cross-section than two or more columns retaining the same outer dimensions of the test rig.

In order to measure the applied force, a load cell is included in the test configuration. Since this requires some electronic readout, the preferred spot to mount the load cell is at the lower part of the test rig. That way, the cables can easily be attached to the rotary table and do not need to hang in free space avoiding possible interference with the X-ray source and the projection directions.

Finally, the actuator may consist of either a manually operated mechanical system or an electrically driven motor. In the following some exemplary configurations as used for fiber reinforced materials are presented to explain some established concepts for in situ CT scanning. In order to classify the configurations, distinction is made between the different load cases.

Tensile or Compressive Load Test

As pointed out in the previous section, the basis for design of load rigs is a cylindrical tube made from a material with low X-ray attenuation able to carry the applied load. Therefore only cross-sectional drawings of the load rigs will be shown in the following. One characteristic difference between the concepts in use is

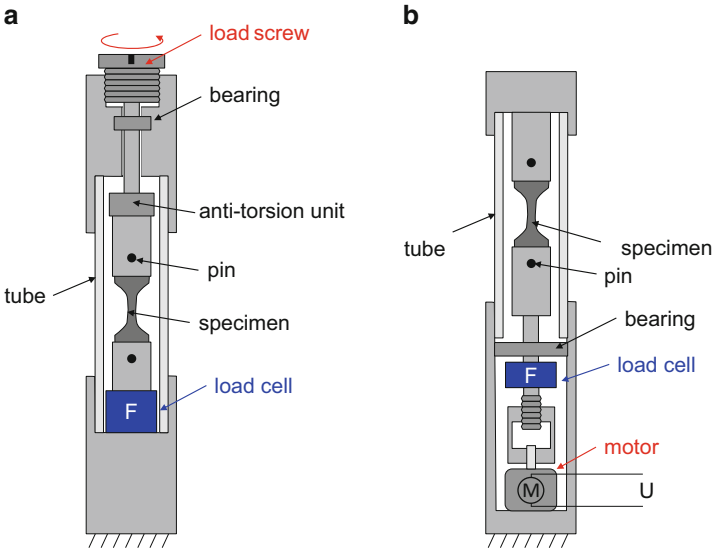

Fig. 6.30 Comparison between manually driven load rig for tensile tests (**a**) and computer-controlled load rig driven by electronic stepper motor (**b**)

the type of load control. While manual load drivers are mechanically more straightforward to implement and more economical, the advantage of a fully load controlled systems certainly is the possibility to automatize the full procedure. In Fig. 6.30 a comparison of two systems as commercially available is shown. Figure 6.30a shows a simple load screw in combination with an anti-torsion unit to stress a specimen pinned to the load rig. This concept is well suitable for isotropic materials causing no failure in the pin section when designing the dimensions of the tapered region and the thickness of the specimen accordingly. The anti-torsion unit is vital in this configuration to avoid any torque being applied to the specimen during the loading procedure. Otherwise superimposed tensile-torsion stress states could be the result, or the mounted specimen could even fail due to excessive torque during load application.

For the configuration of Fig. 6.30b, the specimen is also attached using pins. The basic difference to Fig. 6.30a is the use of an electric stepper motor in combination with a mechanical driver system to stress the specimen in close relation to the operation principle of typical macroscopic load test rigs. Here, the moving part is typically supported by additional bearings and also protected to avoid the occurrence of excessive torque applied to the test specimen. In both configurations, the load applied to the specimen is measured by a load cell positioned at the bottom of the load path.

In contrast to the concepts of Fig. 6.30, for fiber reinforced composites, a different fixture concept was found to be necessary. Similar to macroscopic test specimens, a connection to the load test rig by pins is not reasonable due to shear-out

failure for many laminate configurations. Following the established test standards for tensile or compression testing, the typical approach is to produce tapered test specimens by bonding reinforcements at the end of the specimen. The specimen is then gripped using mechanical or hydraulic jaws to apply load.

In very small load test rigs, the fabrication of jaws comes with some additional challenges, so a more practical solution was found to directly bond the specimen within the load rig using standard two-component epoxy adhesives. Since the duration of one experiment with CT scanning (e.g., hours) largely exceed the duration for bonding and curing (e.g., minutes), this seems to be a reasonable approach. For macroscopic specimens this is quite different because the total test duration is usually within few minutes, and therefore a quick replacement of specimens is appreciated. Using a suitable embedding length of the material within the test rig, this allows failure in the free section and avoids failure of the adhesive bond. A major disadvantage of this concept is the necessity to have replaceable parts of the load rig tensile or compression bars, since the removal of specimen and adhesive from the bars degrades the geometry and therefore requires replacement after few un-mounting and re-mounting cycles. The schematic arrangement of the load rig as used for tensile tests and for compression test of fiber reinforced composites is shown in Fig. 6.31a, b, respectively. Similar to the macroscopic test concepts, one key difference is to keep the free length of the specimen (i.e., distance between edges of lower and upper bar) smaller for compression tests to avoid buckling.

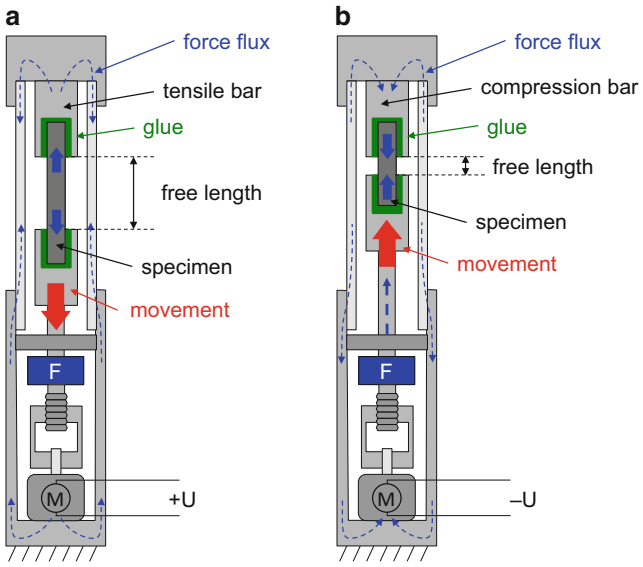

Fig. 6.31 Load rig used for tensile tests (**a**) and compression tests (**b**) of fiber reinforced materials

Mode I Test

As distinct difference to tensile or compression load, the generation of other relevant load states in fiber reinforced composites requires some further modification to the test rigs of Fig. 6.31. As for the macroscopic investigations of laminates, the damage progression under mode I load is of key interest to the design and material optimization of composites. To observe such damage progression with volumetric imaging as offered by CT scanning, the modifications shown in Fig. 6.32 are introduced. In this load rig, the specimen is attached to the lower load bar and moved in the vertical direction. This relative movement may either be due to an actuator at the bottom as seen in Fig. 6.32 or by a load screw at the top as seen in Fig. 6.30a. The material is prepared including a precrack as in the case of macroscopic specimens. At the top load bar a sharp wedge is mounted sliding into the precrack. Due to the steepness of the wedge, the laminate splits and a damage zone develops around the precrack tip.

If the curvature of the wedge is sufficiently large and the material is brittle enough, the crack tip position is sufficiently far away from the wedge tip. Thus the crack progression occurs under a mode I load situation. If the wedge curvature is too sharp, the laminate is instead "cut" and the real load type causing crack progression will likely be a superimposed load state. The force in this configuration is measured at the bottom of the load path and needs to be carefully interpreted since friction effects may add a substantial amount to the force value and thus may not be directly used in the same way as in macroscopic load configurations (i.e., double-cantilever beam configurations). Instead, closer relationship of the mechanical properties is expected to macroscopic wedge-peel tests as carried out for adhesives or thermoplastic tapes [65–69].

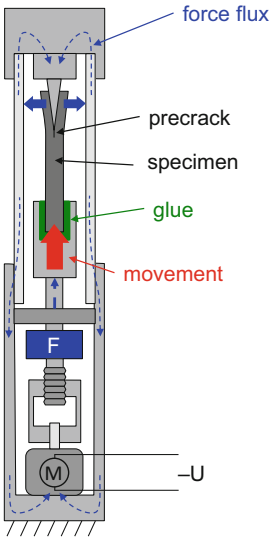

Fig. 6.32 Test rig configuration for wedge-loaded mode I investigation of fiber reinforced materials

Flexural Test and Mode II Test

Another load configuration being distinctly different to the previous cases, the flexural load case is shown in Fig. 6.33. Such loads can either be used to generate flexural stresses or to induce mode II-driven cracks as in the macroscopically applied end-notched flexure specimens. Distinction is made between a load rig applying manual load introduction (cf. Fig. 6.33a) and a computer-controlled system using a motor (cf. Fig. 6.33b). In both cases one challenge is to have supports being present at different positions to allow a deflection of the mounted specimen. Since the support at the center of the tube will always be present within the projected images, the same considerations as for the tube apply. If possible, the material of the support should be affected less by X-rays to assure mechanical stability during exposure, and it should cause a minimum of artifacts. For the case in Fig. 6.33a, the center support is tightly mounted to the tube and therefore remains at a constant position. To introduce a flexural load, two load screws transfer their displacement to the specimen using a slide bearing on which the supports are located. Here one disadvantage is the lack of a proper load cell measurement and the challenge to synchronize the upper and lower load screw in order to avoid skew load situations.

An alternative option is shown in Fig. 6.33b. Here the upper and lower supports remain at a constant position, while the center support is the moving part. By an elongated drill hole within the tube, the support is guided to allow only movement in the designated direction (i.e., the horizontal axis in Fig. 6.33b). Using an actuator

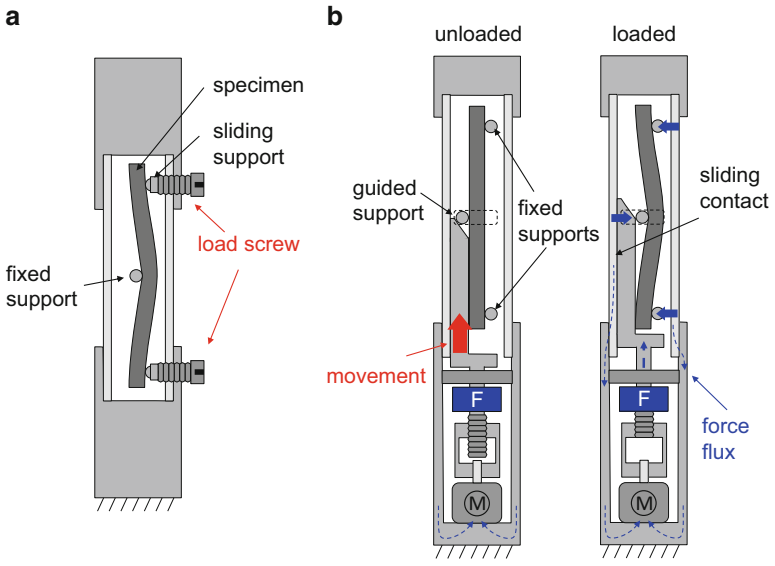

Fig. 6.33 Test rig configuration for flexural testing of fiber reinforced materials using load screws (**a**) and computer-controlled load rig (**b**)

system at the bottom of the test rig, a pull bar is moved in the vertical direction to stress the specimen. A wedge at the tip of the bar allows pressing the support firmly to the specimen and causes deflection. During this operation, the load bar is sliding against the tube, and thus the acting loads are also transferred to the tube in order to avoid significant deflection of the bar itself. The load cell is mounted at the bottom of the configuration to measure the required load. However, this load is composed of contributions due to friction and due to specimen deflection and may not be directly used. Hence using a material with known stiffness for calibration of the system, the measured load may be corrected to obtain true mechanical properties of the measured material.

Thermal Loading

As a fundamentally different type of load source relevant to fiber reinforced materials, a change in temperature may also generate stresses in the material. These stresses are solely caused by the thermal expansion of the material, which may induce some strong gradients in the case of anisotropic materials as in fiber reinforced composite laminates. Moreover, joints between metallic parts and fiber reinforced polymers are subject to a strong gradient in the thermal expansion properties which may induce severe stress at the interface between both materials. Here the basic concept is to generate such stresses in situ to allow accompanied CT scanning. As seen in the schematically drawing in Fig. 6.34, the concept of the test stage is relatively similar to the designs explained in the previous paragraphs. The specimen is mounted at the bottom part and is enclosed in a sealed cylindrical tube made from X-ray stable material. To avoid the occurrence of artifacts, the cylindrical design is kept. To monitor the temperature within the chamber, a temperature element is positioned close to the specimen. Either electric heat elements or Peltiér elements are applied to cause a change in temperature reaching either above or below room temperature.

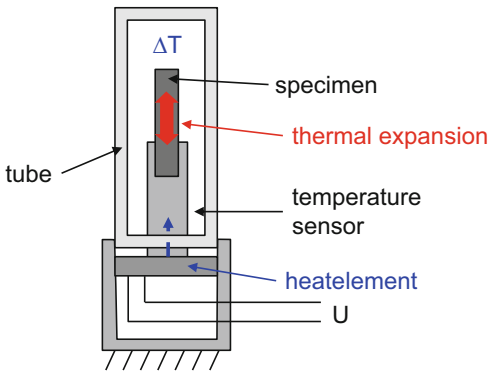

Fig. 6.34 Test rig to generate thermal stress in material specimen

Imaging Requirements

Whatever type of load is being applied to the specimen, one requirement in CT scanning is to have the specimen immobile during the scan duration. Otherwise motion artifacts will appear which may render the measurement useless or cause less detail visibility.

In the case of fiber reinforced polymers, the stress relaxation effect of the matrix system needs to be considered in this context. Consider the load scheme shown in Fig. 6.35 for two subsequent steps of in situ CT scans. The aim is to load a specimen up until a distinct load level F_1 and perform a CT scan at this load level to finish step one. Without material creep, the specimen would simply keep its internal stress state at load F and scanning could be performed immediately. In reality all materials will show some stress relaxation after reaching the programmed load. Hence after the quasi-static load phase to reach F_1 (blue arrows in Fig. 6.35), a wait period needs to be present to allow the material to reach a relaxation load F_1'. At this relaxation load, the CT scan can take place to avoid motion artifacts. Subsequently, the load is further increased to F_2 and the next CT scan is performed in step 2 after allowing stress relaxation of the material to the load level F_2'. This sequence is carried on until the specimen finally fails.

This procedure immediately allows concluding that the mechanical experiments need to be performed in displacement-controlled mode. In force-controlled mode, the material would undergo a more or less constant creep and therefore

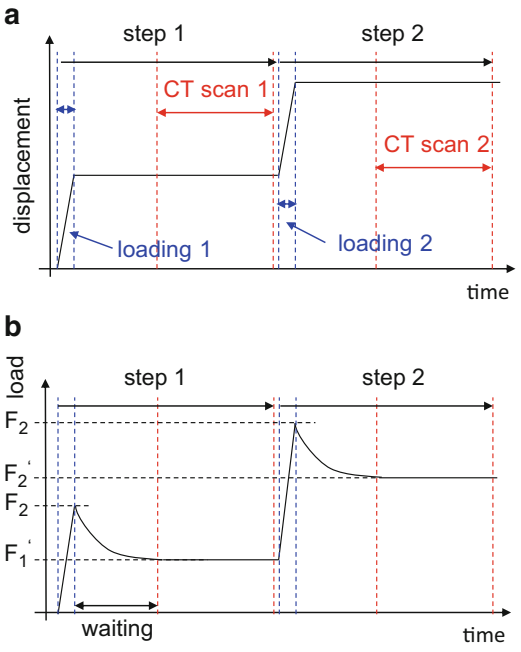

Fig. 6.35 Typical displacement profile (**a**) and load profile (**b**) during in situ CT scanning including effects of relaxation and sequence of actions

continuously deform causing no stable conditions to perform CT scanning. It should be noted that the ratio of durations for loading and scanning is not to scale from Fig. 6.35, since the CT scan operation may easily fall in the order of hours, whereas the load duration typically still is within a few minutes. Also the level of stress relaxation is exaggerated for better visibility. However, careful considerations are required when interpreting the imaged damage state. Firstly, the quantified dimensions and corresponding stress-strain states might be of reduced amount, since the specimen undergoes relaxation prior to scanning. Secondly, upon subsequent loading, the material starts from a different stationary state, so the material behavior concluded from such interrupted load profiles may be altered compared to the conclusions drawn from continuous load profiles until failure.

6.4 Digital Volume Correlation

The approach to use the correlation of a sequence of digital images is already well established and is being applied more and more in material testing applications. Volumetric imaging-based X-ray computed tomography [25, 26, 31, 34, 35, 40, 46–61], magnetic resonance imaging [70], or, for partially transparent or opaque materials, laser confocal scanning microscopy [71–75] are also used frequently. Based on the volumetric image information, a consequent extension of the digital image correlation method presented in Chap. 3 was suggested by Bay et al. [76]. They were among the first to consider the correlation of two subsequent volume images [76]. This method of DVC allows to measure quantitatively the 3D internal displacement and deformation of a material. The main distinction between approaches of 2D-DIC, 3D-DIC, and DVC is shown in Fig. 6.36. The primary difference between DIC and DVC is the hierarchy of information derived from the measurement. In simple 2D-DIC, a plane surface measurement is performed, not being able to detect out-of-plane components w and thus resulting in simple 2D

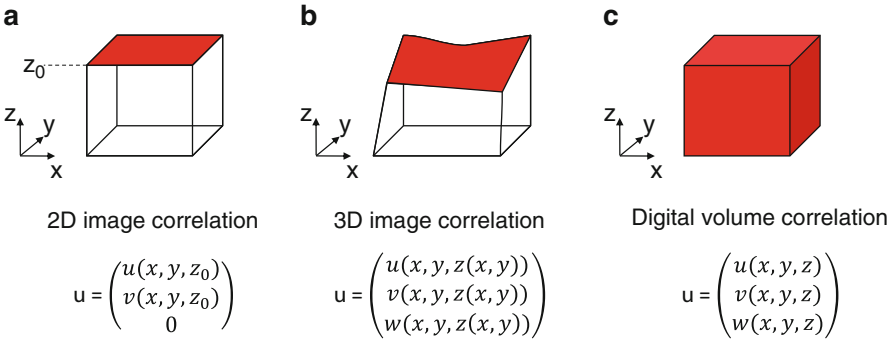

Fig. 6.36 Comparison of displacement vectors $\boldsymbol{u}$ as obtained from 2D-DIC (**a**), 3D-DIC (**b**), and DVC (**c**) including schematically representation of information hierarchy

displacement information $\boldsymbol{u}$ of the outer surface. The extension to 3D-DIC allows measuring the out-of-plane component of the displacement and results in a 3D displacement measurement $\boldsymbol{u}$ of the surface. For the DVC approach, the displacement is not just measured at the surface of the material but originates from the full volume and therefore constitutes a true 3D measurement of the displacement vector $\boldsymbol{u}$ in every point of the volume.

Among the applications of the DVC technique, there are obvious candidates like the ability to validate the result of 3D-FEM computations. Successful applications include materials such as wood [41, 42, 49] and composite materials [58].

In full analogy to the procedure used in DIC, the basic steps for DVC are the following:

1. First recording a volumetric image of the material
2. Deforming the volume due to applied loads
3. Second recording of a volumetric image of the material
4. Correlation of both volumetric images using subvolumes and computation of displacement vector for each subvolume

The acquisition of a volumetric image and the in situ deformation of the material were presented throughout Sects. 6.1, 6.2, and 6.3, and the only remaining step now is the correlation of two volumetric images. The basic concept is shown in Fig. 6.37. Since a computation of the displacement vector of a single voxel is not suitable due to the ambiguity faced in the image correlation process (cf. Sect. 3.1), a local neighborhood around one voxel is used. As seen in Fig. 6.37, in DVC this is a local subvolume subset rather than a 2D subset as introduced for DIC. Apart from that, the subvolume is subject to a general displacement, rotation, and deformation as introduced in DIC before.

In order to perform the correlation process in DIC, speckle-type patterns are applied to the inspected surface to provide locally unique subsets. Since such application of speckle patterns is not possible in the interior of the material, other image signatures are required to perform the correlation process. To this end, the material microstructure itself can be used to provide a unique correspondence of

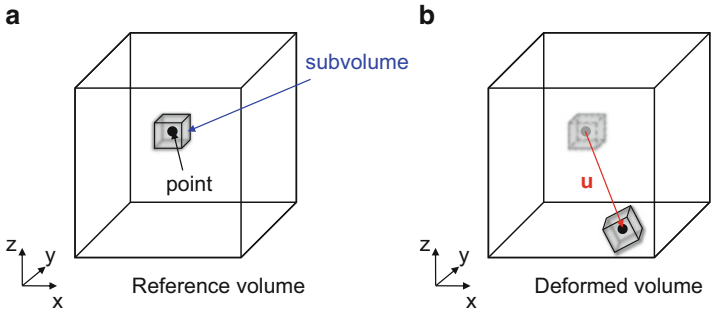

Fig. 6.37 Tracking deformation states between reference volumetric image (**a**) including local volumetric neighborhood (subvolume) and deformed volume (**b**) as being used for DVC

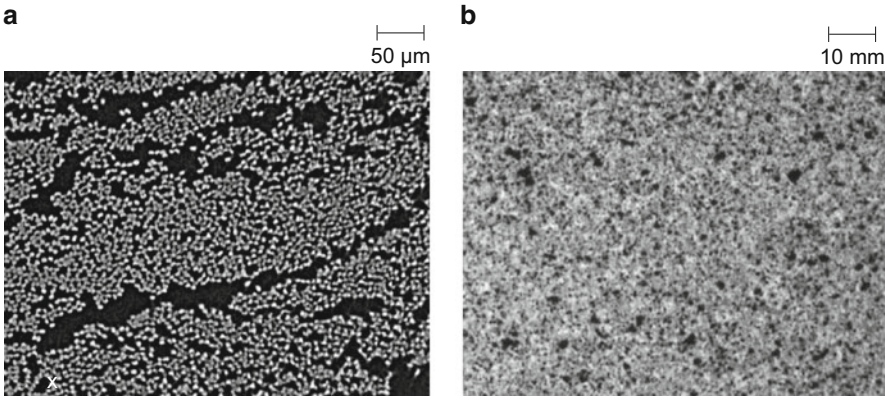

Fig. 6.38 Examples of CT cross-sections of fiber reinforced material (**a**) and typical speckle pattern used in DIC (**b**)

subvolumes. For some materials a stochastically distribution of particles or voids is found on the microscale. Accordingly, subvolumes of such materials yield unique information to perform a correlation process. For fiber reinforced materials, the arrangement of the fiber filament cross-section is of such a length scale to allow successful DVC [58]. A comparison of two cross-sectional images of a fiber reinforced material in Fig. 6.38 to a speckle-type pattern reveals the close similarities.

Although the principle of DVC constitutes a straightforward extension of the DIC approach, one of the key differences is the computational intensity faced. To this end, further distinction is required between two typical implementations of DVC. The first algorithms developed were based on a correlation procedure using only discrete voxel sizes. This comes with lower computational intensity and is readily be implemented by search algorithms in the spatial [76] or frequency domain [74]. However, this allows a calculation of the displacement vector only by increments of more than half the voxel size, which is typically not feasible for many materials being subject to small deformations only. Thus the strain resolution of this simple implementation would be 16.7 % strain for a 3-voxel cube, 10.0 % strain for a 5-voxel cube, 7.1 % strain for a 7-voxel cube, and so on. For the typical strain values in the linear elastic range of many materials with fractions of 1 %, a sub-voxel accuracy of the correlation procedure is required. Therefore, the present focus of the method development is on the improvement of the algorithms used for such sub-voxel correlation [76–81]. Since an extensive discussion of the image correlation algorithms is beyond the scope of this book, the reader is referred to [82] on the basics of image correlation and to Pan et al. [77] for a recent review and modification of existing correlation algorithms.

To demonstrate the use of this method, Figs. 6.39 and 6.40 show some exemplary results of volume cross-sections as collected from an in situ CT scan of a carbon fiber reinforced epoxy material. Following the procedure outlined in

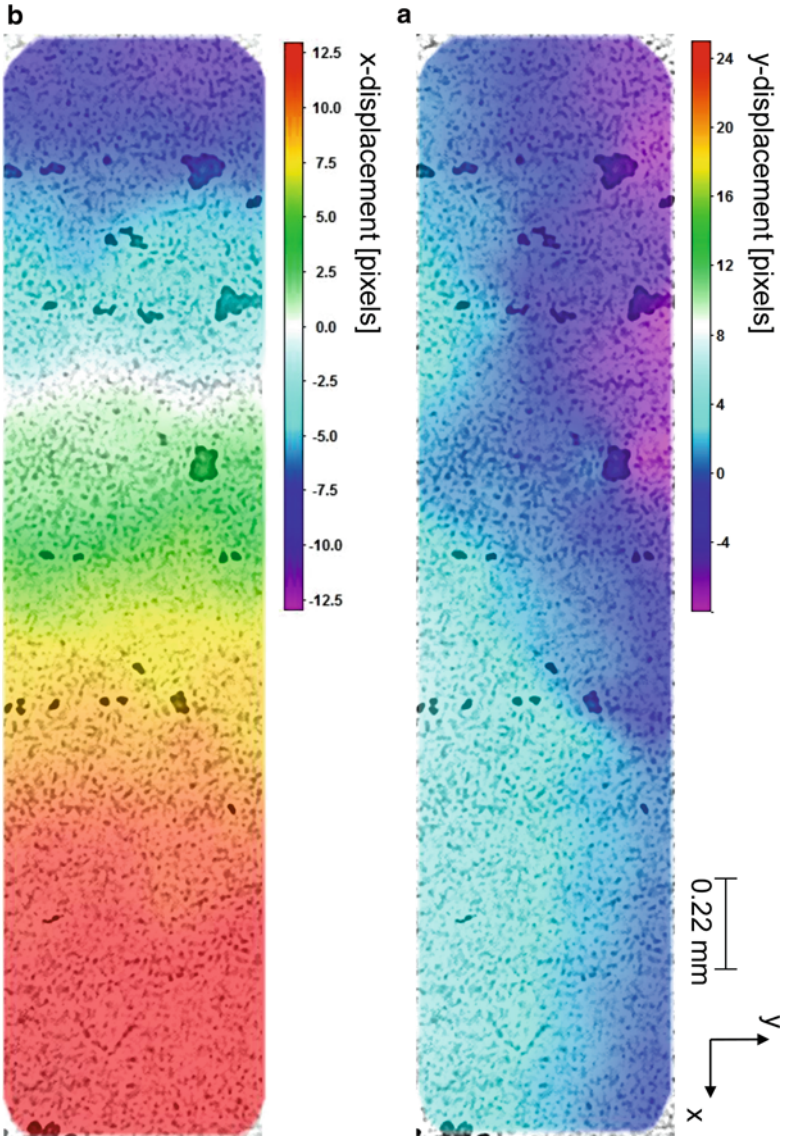

Fig. 6.39 Arbitrary *xy*-cross-section out of volumetric image of in situ loaded fiber reinforced polymer. Computed displacement fields in *y*-direction (**a**) and *x*-direction (**b**) are superimposed to the CT cross-sectional image

Sect. 6.5.2.1, miniaturized specimens were prepared and loaded by a compressive force in situ in parallel to the *y*-axis. CT scans were performed in the initial state and at a load level prior to ultimate failure. For the DVC process, the software package DaVis was applied, and the resultant displacement field is visualized as

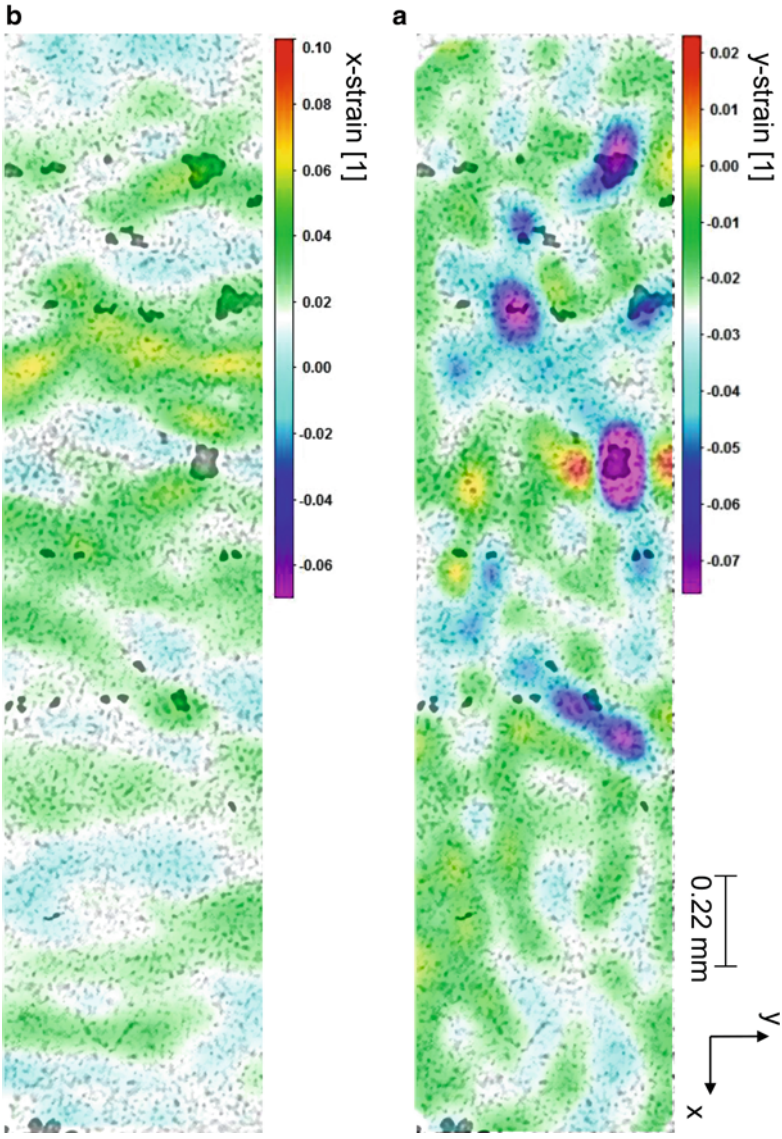

Fig. 6.40 Arbitrary *xy*-cross-section out of volumetric image of in situ loaded fiber reinforced polymer. Computed strain fields in *y*-direction (**a**) and *x*-direction (**b**) are superimposed to the CT cross-sectional image

x-displacement and *y*-displacement in Fig. 6.39 superimposed to the selected cross-section. For technical reasons, the displacement scale is given in pixels with one pixel corresponding to 1.36 µm. As seen from the black regions in the *xy*-slice, the material includes several voids of diameters up to 100 µm. In the computed displacement field, the material predominantly shows the compression due to the

applied compressive force in *y*-direction and the effect of Poisson's contraction in the *x*-direction. For the corresponding local strains shown in Fig. 6.40, the situation is different. Here the larger voids show a significant strain concentration indicating regions of higher compliance. As will be seen from the analysis of the failure modes in Sect. 6.5.2, these regions form a weak link in the material contributing significantly to the final failure mode. Similar to the analysis of DIC images presented in Chap. 3, this analysis can thus be used to identify strain concentrations in the volume of a material to perform assessment of possible failure locations prior to failure or to analyze the evolution of failure initiating at such spots.

6.5 Application to Composites

The use of computed tomography to inspect the microstructure of fiber reinforced materials has been outlined in the previous sections. Based on the scope of the book, the last section of this chapter has its focus on capabilities of the method to detect and quantify damage initiation and damage progression. Thus only exemplary applications related to in situ testing and ex situ testing approaches are presented in the following. Other fields of application of computed tomography as relevant to composites such as porosity quantification or measurement of fiber orientation are instead covered by recent literature [16–24].

Before proceeding to the first subsection on ex situ testing approaches, a brief introduction to the use of segmentation tools to visualize the internal microstructure is given. This step is necessary to provide the basic analysis routines used to evaluate the damage progression as presented in Sects. 6.5.1 and 6.5.2.

As discussed in Sect. 6.1 and 6.2, the gray scale images obtained in computed tomography basically represent the material density. In the absence of image artifacts and for reasonable resolution, this may thus be used to segment different materials based on their difference in density. A trivial example for this procedure is given in Fig. 6.41. The selected *xz*-slices of a computed tomography scan result from an inspection of a Sigrafil CE1250-230-39 prepreg fabricated with consolidation pressures below the manufacturer recommendations. Due to the missing pressure, this results in the formation of pores upon curing and is readily visible in Fig. 6.41. Both laminates were scanned at a time, so the histogram of gray values on the left side of Fig. 6.41 is representative for both laminates. Within the histogram two clear peaks are found, which correspond to the density values of air and the composite material. Based on the large distances of the peak maximums, it may seem trivial to segment this image. The threshold of Fig. 6.41a is thus selected at the half distance between both peak maxima. The corresponding segmentation is indicated as yellow line in the *xz*-slice in Fig. 6.41a on the right side. Obviously, some of the needle pores in the lower laminate are not segmented correct. This is due to the presence of image artifacts as discussed in Sect. 6.2, causing slightly different gray values for the case of air enclosed by the composite material. By moving the segmentation threshold towards the material peak, more

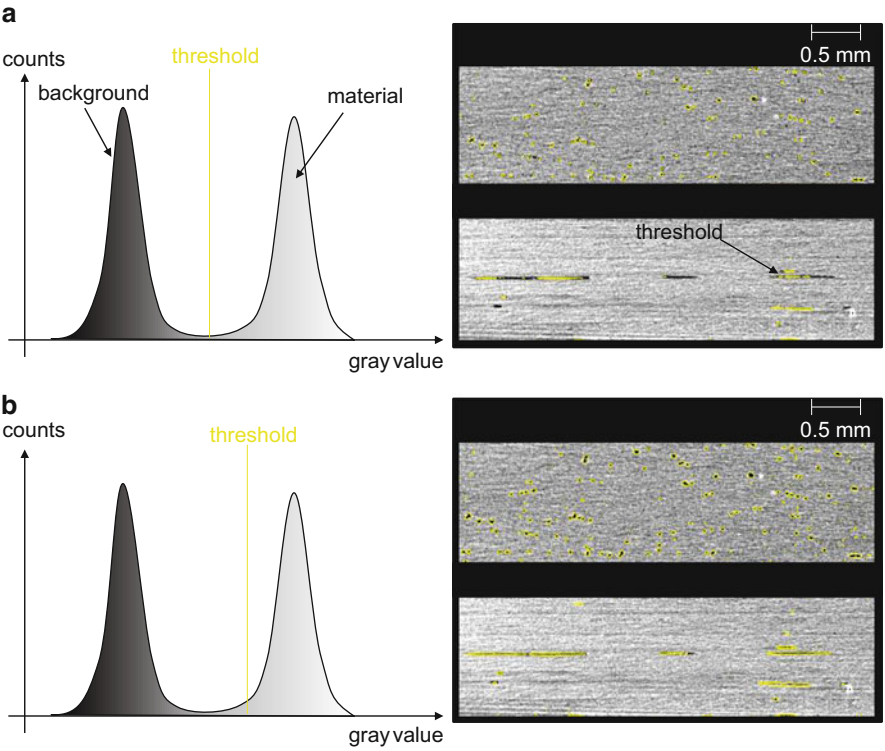

Fig. 6.41 Selection of threshold for image segmentation at half distance between peak maxima (**a**) and close to material peak (**b**)

realistic segmentation is reached as seen in Fig. 6.41b. Since this procedure is driven by visual decision criteria, its suitability for extraction of quantitative information is generally questionable. Consequently, various strategies to obtain valid decision boundaries have been proposed in literature. Recently, this has seen a strong focus on the application to quantify the degree of porosity as well as to segment matrix and fibers [16–24]. Despite of these strong research efforts, there is still no standardized procedure to perform image segmentation in computed tomography, and consequently, extraction of quantitative volumetric information is still challenging.

After image segmentation, there is a broad range of possibilities to analyze and interpret the data, ranging from simple volumetric ratios to topological analysis. As an example of both, the two laminates of Fig. 6.41 alongside with a reference laminate are subject to a topological analysis with their results shown in Fig. 6.42. On the top of Fig. 6.42a–c, the 3D visualization of the inspected laminates is shown. All three laminates were scanned at the same time and are segmented using the threshold of Fig. 6.41b. At the bottom of each figure, a topological analysis is shown for the detected porosity. The false-color range indicates the volumetric size

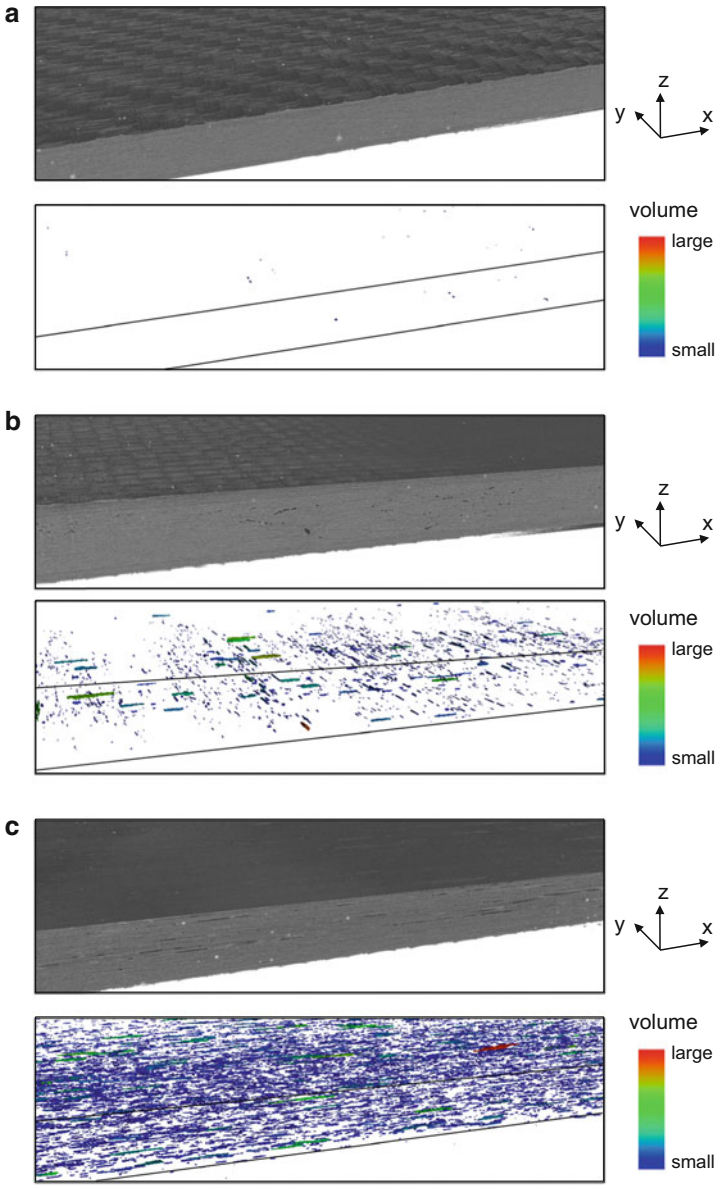

Fig. 6.42 Visualization of porosity for well-consolidated laminate (**a**), laminate with some needle pores (**b**), and laminate with extraneous porosity (**c**)

of the single pores (or the pore network if existent). As additional guide to the eye, two black lines are added to the figures, representing the edges of the laminates. A reduced consolidation pressure results in the formation of a substantial amount of needle-shaped pores (cf. Fig. 6.42b) in combination with extraneous porosity

(cf. Fig. 6.42c). Despite of the difficulty to extract quantitative information from these measurements, the visualization of these voids prior to testing certainly helps to assure that the specimen is free of porosity as for the laminate of Fig. 6.42a. However, it is important to mention that the scan resolution will obviously influence the porosity assessment as well. As demonstrated by Kastner et al. [21], the voxel resolution as well as the choice of the threshold will have tremendous impact on the quantified porosity. Thus, the choice of scan parameters as well as the size of the test specimen will need to be considered for such analysis routines.

In the context of damage assessment, it is worth noting that it is generally hard to distinguish between the indications of porosity and those given by the formation of cracks. This is owed to the fact that cracks in the composite material are basically air inclusions of a certain shape and orientation. Since the visualization of these indications is based on their density, it is thus impossible to separate both indications without further knowledge. As practical example for this challenge, a 3D visualization of a tapered section of a laminate is shown in Fig. 6.43. This scan visualizes the tapered section of a Sigrafil CE1250-230-39 prepreg test specimen of $[(0/90)_2]_{sym}$ stacking sequence fabricated with interspersed plies as described in Sect. 4.7.3.2.

The specimen was subject to a tensile load until failure within the reduced section (not shown in Fig. 6.43). For Fig. 6.43b, the gray value range of the composite material is chosen transparent, so that only the volumes with density close to air remain. For improved visibility, the air volume surrounding the specimen was also chosen transparent, so only enclosed air volumes remain visible in

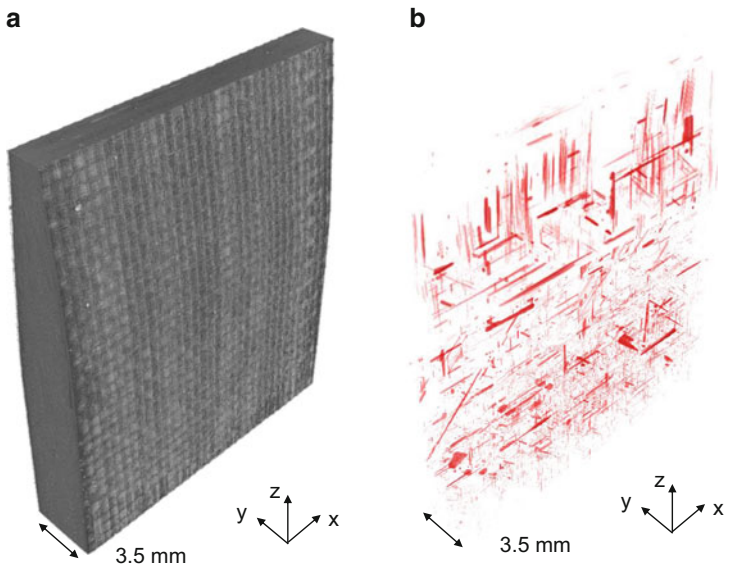

Fig. 6.43 3D CT scan of tapered laminate section (**a**) and visualization of cracks and porosity by setting composite material and surrounding air transparent (**b**)

Fig. 6.43b. This kind of visualization allows evaluating the orientation and position of pores and cracks. However, there is no way to distinguish between the occurrences of either kind. The laminate has certainly seen some damage in the scanned region before final failure of the specimen, so parts of the indications of Fig. 6.43b are due to the presence of cracks. But as evident from computed tomography scans prior to testing, there is always a certain amount of pores in the reinforcement section, which is difficult to avoid by the chosen processing conditions. Hence, a considerable amount of the indications of Fig. 6.43b are due to needle pores. Because of their shape and orientation in parallel to the fibers of the individual plies, it is not possible to distinguish them from the occurrence of inter-fiber cracks. Also, it is likely, that the presence of a pore acts as initiation site for an inter-fiber crack. Consequently, mixtures of both indications are also likely to occur.

Thus for damage assessment by computed tomography, the following procedure is recommended:

1. Inspection of the relevant part of the test specimen prior to mechanical testing to assure there are no significant pores or other inclusions
2. Comparative inspection after testing of same part of the test specimen

This procedure allows evaluating the difference before and after testing and thus may be used to resolve the ambiguity of indications. In cases of almost negligible indications prior to testing (such as in Fig. 6.42a), the indications after testing may be directly used to perform damage assessment.

6.5.1 Ex Situ Testing

Based on the consideration presented in Sect. 6.3, it is suitable to distinguish between inspection approaches performed ex situ and in situ. For the ex situ approaches, the specimen is loaded in an external universal test machine until a certain damage state is reached. Subsequently, the specimen is dismounted and inspected by a CT scanner. Depending on the type of analysis, the specimen is then mounted again in the universal test machine and loaded until the next damage state is reached. In contrast, in situ approaches combine the capabilities of a universal testing machine with a CT scanning device and are described in their applications in Sect. 6.5.2.

6.5.1.1 Visualization of Damage Progress

In this subsection exemplary applications for tracking of damage progress using ex situ CT approaches are shown. Since there are numerous applications found in literature that could be added to this section [25, 26, 31, 34, 35, 40, 46–61], focus will be given on two representative examples. As first example, the growth of a mode II interlaminar crack is investigated. This kind of example is representative

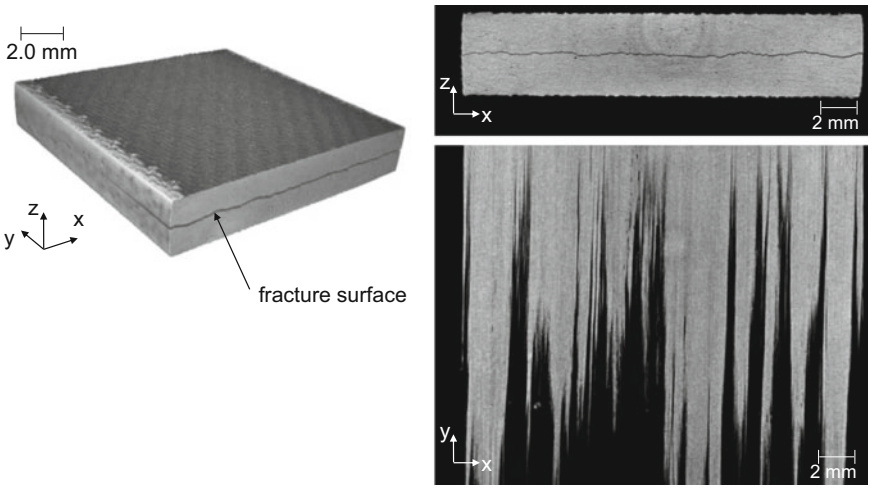

Fig. 6.44 3D visualization of mode II fracture surface in unidirectional laminate and according cross-sections in *xz*-plane and *xy*-plane

for a macroscopic indication and is used to demonstrate some basic concepts in tracking of damage progression. As second example, the growth of inter-fiber cracks in cross-ply laminates is presented. For this example, the major challenge stems from the visualization of relevant indications and the compromise between high image resolution and large inspection volume.

As first example, a typical specimen as used in end-notched flexure test to determine the mode II fracture toughness is analyzed (cf. Sect. 4.7.2.2). In this configuration the crack initiates at the precrack position and starts to grow interlaminar due to the applied bending load. The typical appearance of the fracture surface after testing is shown as 3D volume in Fig. 6.44. The *xz*-cross-section and the *xy*-cross-section of Fig. 6.44 are used in addition to visualize the complexity of the fracture surface achieved in this test condition. For this unidirectional prepreg laminate fabricated out of the Sigrafil CE1250-230-39 material, the crack growth in mode II condition causes splitting of the laminate in parallel to the fiber axis. Thus, the real crack front is hardly described as an ideal rectangle, but has certain waviness along the *z*-axis. In addition, the crack extends to different distances along the *y*-axis depending on the *z*-position.

In order to evaluate the damage progression during the mode II test, the specimen was first scanned directly after precracking and a second time after the first load drop according to the evaluation procedure of ASTM D7905. A comparison of both scans is shown in Fig. 6.45. For this visualization, the composite material and the surrounding air volume were chosen transparent, so that only indications of the enclosed volume remain visible. To improve the visibility of the crack front, a small wedge was inserted at the precrack position to open the interlaminar crack during the CT inspection. For the evaluation the 3D result is projected to the *xy*-plane rendering all indications semitransparent.

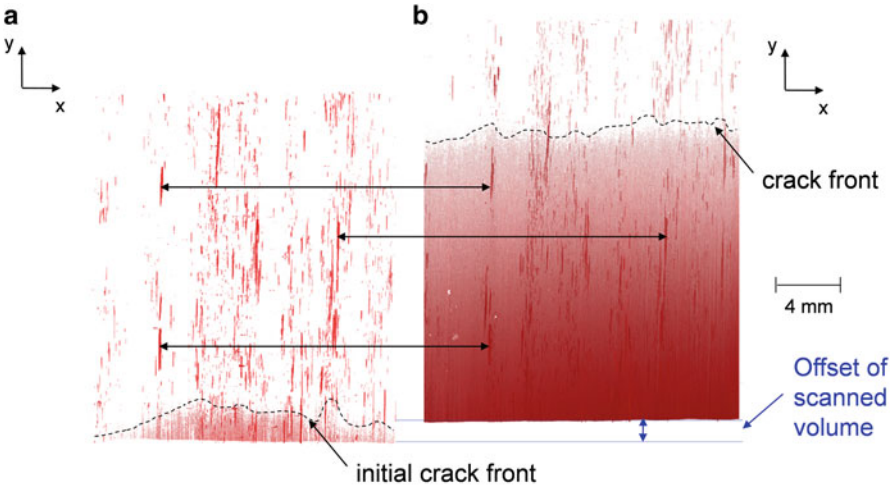

Fig. 6.45 Comparison of mode II fracture surface in unidirectional laminate after precrack procedure (**a**) and after mode II ENF test (**b**) using visualization of cracks and porosity by setting material as transparent

The position of the crack front after precracking is marked as dashed line in Fig. 6.45a. There is not a plane crack front, but a distinct profile with different crack extension along the *y*-axis as function of the *x*-position. Also, there is a certain level of pores readily visible inside the laminate. In this application they were found to be quite useful, since their shapes can be used as characteristic fingerprint to determine the offset between the first scan and the second scan as indicated by the black arrows of Fig. 6.45. During the mode II test procedure, the crack front advances by 17.4 mm in average as seen from Fig. 6.45b. The crack front retains a distinct profile. A 3D evaluation of the newly generated crack surface of Fig. 6.45 allows to quantify the total crack surface, which evaluates as 1074 mm^2 for the case shown. Unlike other attempts to measure crack lengths using X-ray projection methods, the use of the 3D volume considers the full topology of the crack surface and therefore especially considers the waviness along the *z*-axis. For metallic materials such approaches have already demonstrated their capabilities for quantitative estimation of mixed-mode load conditions [83, 84]. The quantification based on visual observation of the crack front (averaged at both edges) according to the ASTM D7905 results in 348 mm^2. Thus the real fracture surface is underestimated by a factor of 3. However, the data reduction routine in ASTM D7905 does not directly apply the value of the fracture surface and, hence, does not benefit from such improved evaluation methods. Instead, the volumetric measurement of the fracture surface may constitute an alternative approach of fracture toughness determination in the spirit of Griffith's energy relation.

As further example, the growth of an inter-fiber network in cross-ply laminates is presented. The damage sequence recorded for a $[0/90_3/0]_{sym}$ laminate made from

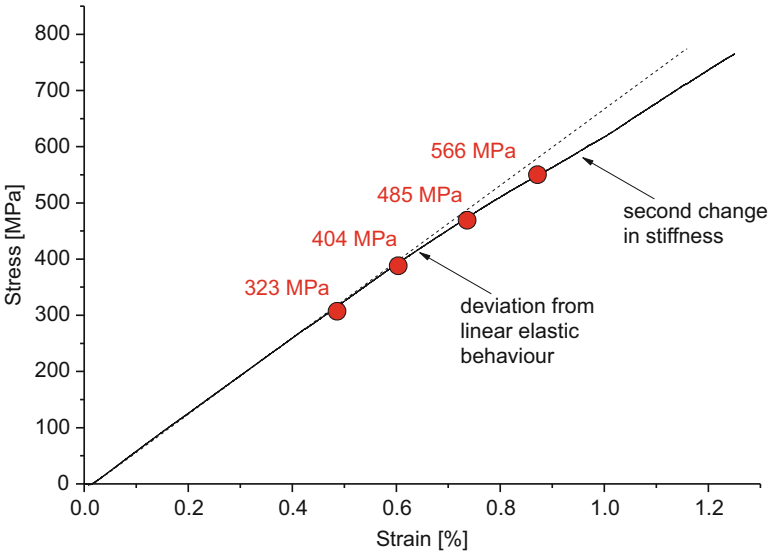

Fig. 6.46 Stress-strain curve of exemplary $[0/90_3/0]_{sym}$ specimen with levels of CT inspection marked in *red*

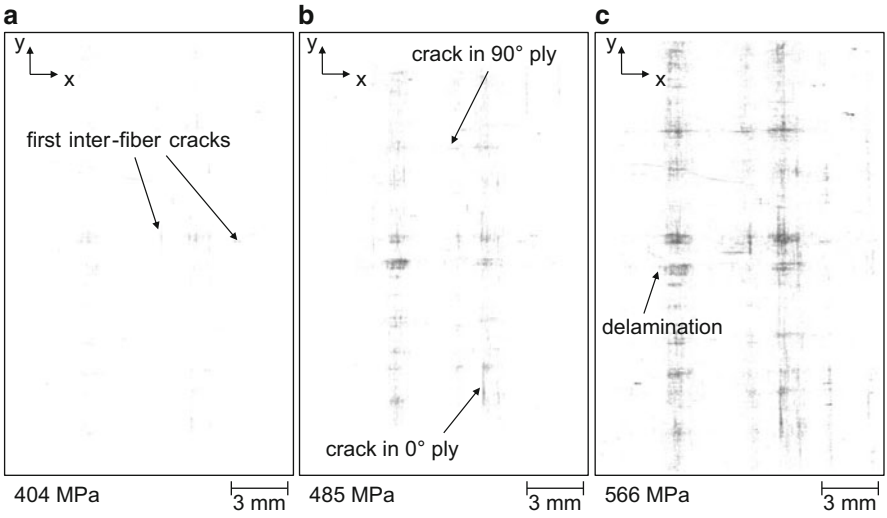

Fig. 6.47 Sequence of images recorded at distinct stress levels shown as projection of the 3D volume to the *xy*-plane with material set transparent

Sigrafil CE1250-230-39 prepreg subject to the load profile shown in Fig. 6.46 is given in Fig. 6.47. The specimen was loaded along the *y*-axis to the first level of 323 MPa, unmounted from the test machine and then scanned using the computed tomography parameters given in Table 6.1. Subsequent to the scan, the specimen

was remounted and loaded until the second stress level of 404 MPa is reached. These steps are repeated until reaching the stress level of 566 MPa. As seen from the stress-strain curve of a specimen from the same plate loaded until failure, there are several changes in specimen stiffness, which can readily be associated with microstructural changes within the materials, such as crack formation.

In Fig. 6.47, the scans are shown as projection of the scanned volume to the *xy*-plane following the visualization described above with the composite material set as transparent. Since almost no porosity was observed in the scan at the lowest stress level of 323 MPa, all indications visible in Fig. 6.47 may readily be understood as formation of damage in the material.

In Fig. 6.47a, recorded at the region of first nonlinearity of the stress-strain curve, the formation of a microscopic crack network occurs. This is indicated by the light black lines in the *xy*-projection, corresponding to the formation of first inter-fiber cracks in the 90° and 0° plies. At increased stress levels, the black indications densify at the previous positions and appear at new locations (cf. Fig. 6.47b). Depending on the orientation of the lines, these may readily be correlated to the occurrence of further inter-fiber cracks, which can be related to their specific depth position by the inspection of the 3D volume. Some areas show larger black clouds extending from the position of previously grown inter-fiber cracks. These areas are located at the depth positions between the individual plies and may thus easily be understood as formation of delamination. At highest stress levels, a significant amount of microscopic damage has already been accumulated and has led to the formation of the crack network seen in Fig. 6.47c. In addition to numerous inter-fiber cracks along the 0° and 90° directions, there is a substantial area showing inter-ply delamination. Beyond this stress level, the damage is expected to accumulate further and finally cause the rupture of full plies. Since this is typically not compensated by the remaining plies, this will ultimately cause the rupture of the full laminate.

Thus for stress-strain curves with significant signatures as seen in Fig. 6.46, the direct transfer of those procedures to other load scenarios, specimen types, and material combinations is straightforward. However, depending on the selected CT scan parameters, the presence of image artifacts, and the volume size, it may result in less visible details. Also, for several applications no significant deviations of the stress-strain behavior from linearity occur prior to ultimate failure. To this end, Sect. 7.2.4.1 presents a suitable combination between acoustic emission analysis and CT to deal with such conditions.

6.5.1.2 Extraction of Geometries from Volume Data

Apart from visualization of damage progression itself, the extraction of existing damage from volumetric images can be used as input for modeling approaches.

The application of computed tomography to perform dimensional measurements is already standard in quality control and has seen a long history of developments. Using the image segmentation methods presented above, it is feasible to extract 3D

representations of the segmented entities. This process is known as reverse engineering and is referring to the creation of a digital dataset based on the physical representation of the object. Compared to alternative methods, like tactile or optical measurement systems, computed tomography comes with the large benefit to also show internal structures and thus allows virtual disassembly of parts. The outer contour of these parts can be directly turned into point clouds or into tessellated surfaces (e.g., as triangulated STL files). These files can then be compared relative to a CAD drawing or may be used to inspect the dimensional accuracy of a part [5].

In the context of damage tracking followed herein, these possibilities are consequently extended by the extraction of crack geometries as digital objects for damage progression modeling or for validation of measurement methods. To this end, two examples are presented in the following to demonstrate the possibilities of this approach for assessment of material failure.

In a first example, the extraction of a fracture surface of a mode II crack is presented. As schematically shown in Fig. 6.48, the full procedure basically consists of two subsequent steps. In the first step, the crack surface is extracted from a CT scan and digitized to yield a digital representation of the 3D geometry. Within the second step, this digital object is imported to a FEM program and embedded to a CAD object for further processing. Although these steps are conceptually easy to follow, the practical handling of the surface extraction, digitization, and embedding comes with several challenges and may result in inaccuracies if carried out inappropriately. Thus, the sequence is described in more detail in the following using

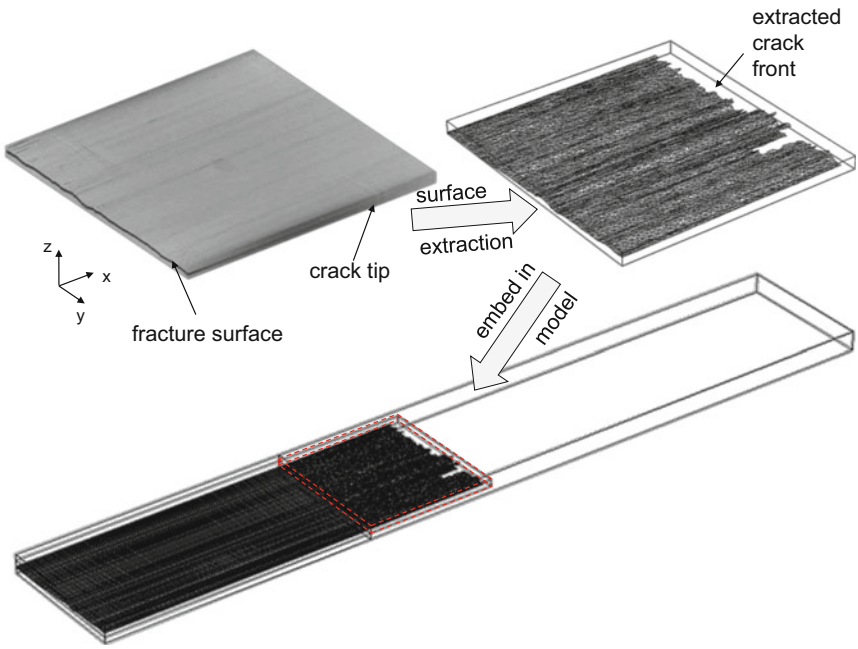

Fig. 6.48 Scheme of procedure used to transfer CT scan of fracture surface into FEM-model

the software packages VGStudio MAX, MeshLab, and COMSOL Multiphysics as representative tools to perform surface extraction, mesh processing and geometry embedding, and FEM computation.

To extract the fracture surface, a suitable CT scan of the region surrounding the damage zone is performed. In this context, the volume may already be reduced to yield only the region of interest close to the fracture surface for further processing as seen in Fig. 6.48.

The CT scan should be of sufficient resolution and contrast, to allow proper image segmentation using the threshold techniques discussed in the beginning of Sect. 6.5. For proper extraction of the crack tip geometry, the selection of the segmentation threshold is of particular relevance and should be considered in detail when performing the segmentation step (cf. Fig. 6.49). In this context it is worth noting that most of the postprocessing steps cause a reduction of the volume of the extracted geometry. Thus shrinkage of the extracted object is technically possible, while artificial growth of the geometry is generally not deemed a feasible approach. As a consequence, the threshold selection should be carried out in a way to slightly overestimate the crack front position as seen in the example of Fig. 6.49c. Within VGStudio MAX it is possible to perform a surface extraction step using thresholding techniques. The obtained segmentation boundary can then be exported as STL file format to yield a tessellated surface for further processing. In this context, a "normal" level of detail was found to be appropriate for the surface extraction algorithm in VGStudio MAX. Nevertheless, a high level of accuracy in

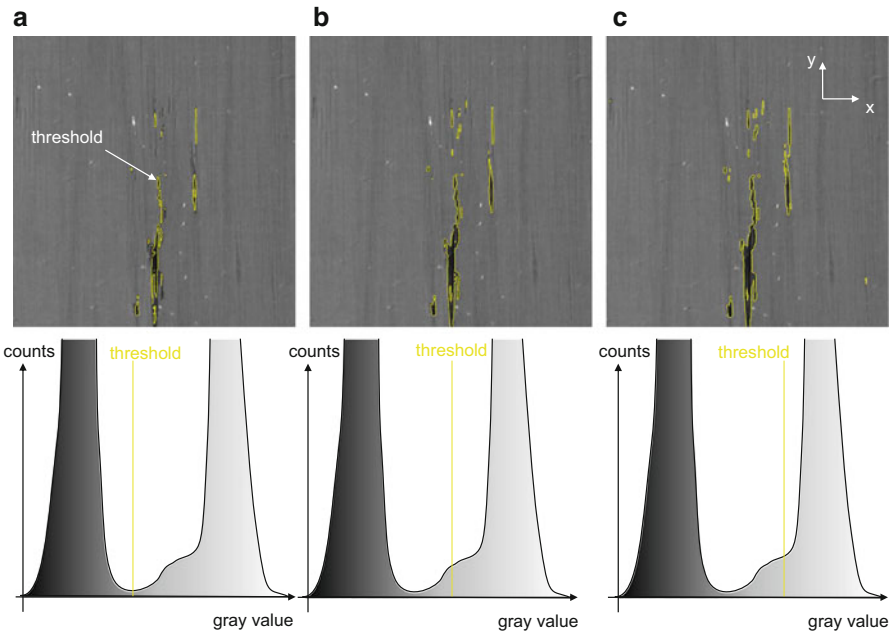

Fig. 6.49 Influence of selected threshold on geometry of crack tip

this step may result in large files for further processing and may need adjustment subject to the extracted volume, scan resolution, and computational capabilities for processing.

As next step, the obtained STL file typically needs further processing before used in a FEM environment. This is mostly due to several issues arising from the tessellation algorithm applied to the extracted surface. First, there is a large likelihood that the obtained fracture surface is not fully closed, which is caused by imperfections of the CT scan as well as the selected segmentation threshold. Such holes need to be closed, to yield an appropriate representation of the fracture surface. Second, the tessellation algorithm is likely to generate topologically non-manifold faces and vertices in regions of geometric singularities (i.e., at the crack tip). Since these cause difficulties for generation of computational meshes, these need to be removed as well. And finally, the presence of pores or crack bifurcations may cause isolated entities, which may be considered in FEM approaches, but may also lead to difficulties in mesh generations. Thus it was found to be useful to remove such isolated surfaces before further processing.

Since all these operations are hardly implemented by manual mesh processing strategies, they require an appropriate environment to perform such STL file modifications. To this end, the software platform MeshLab was used for processing and simplification of the extracted surface.

After import of the STL file, the first step consists of a removal of isolated entities by the command "remove isolated pieces" applied to the imported mesh. Based on the selected option, this is used to remove all isolated objects depending on their diameter or number of faces as seen in the transition between Fig. 6.50a, b.

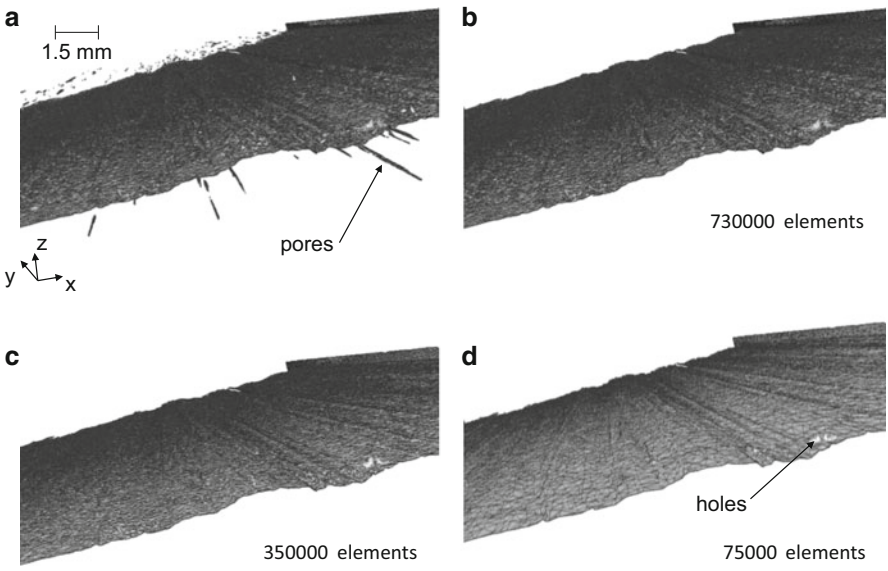

Fig. 6.50 Use of "remove isolated pieces" command to remove isolated entities (**a**) and "quadratic based edge collapse strategy" to simplify the mesh to different number of elements (**b–d**)

For further processing within a FEM program, the topology of the obtained mesh may need some processing. Some of the mesh refinement strategies present in the next steps will require a mesh with two-manifold edges. This means that each edge should be connected to exactly two neighboring faces. Non-closed objects are typically one-manifold (or even zero-manifold for plane edges) and objects containing artifact faces are three- or more manifold. Before further processing, the vertices, edges, or faces causing this lack of topological integrity of the surface need to be removed. Examples for such non-two-manifold edges are enclosed faces or overlapping faces. These are difficult to spot by the bare eye, but are easy to select and delete by using the "select non-manifold edge" filter. Careful removal without compromising the integrity of the geometry is used to yield a suitable mesh representation for further processing.

Subsequently, the mesh is subject to a simplification scheme. Among the different choices, the "quadratic based edge collapse strategy" option following the scheme of Hoppe was found to be particularly useful [85]. Two stages of mesh simplification are seen in Fig. 6.50c, d as compared to the exported mesh from VGStudio MAX in Fig. 6.50b. For such mesh refinements, it is key to preserve the topology of the extracted surface and to avoid removal of geometric details, which are required for the computation result. The latter aspect is hard to determine at this stage, so the simplification routines should be evaluated in their impact on the computation results by comparing results of different simplification levels. Clearly, this step is used to increase the numerical efficiency of the modeling procedure and should thus be considered carefully to reach a satisfying level of detail, while keeping the numerical intensity at a minimum. Newly generated or existing holes are filled using the "fill holes" or "close holes" command as shown in Fig. 6.51. Since a fracture surface is by definition free of holes, the latter is a requirement for further computation tasks. As final step, the simplified and repaired surface is exported to another STL file.

Within the FEM program COMSOL Multiphysics, STL files may be imported during geometry creation. For the exemplary fracture surface of a mode II crack, only the crack tip was scanned by CT and is imported into the FEM program. The remaining parts of the specimen may either be imported from other CAD formats or

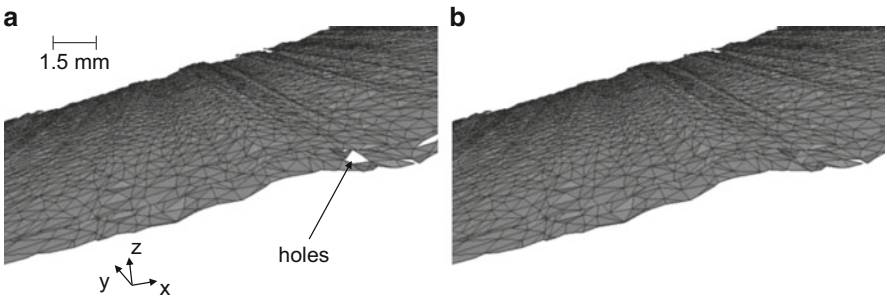

Fig. 6.51 Use of "fill holes" command to artificially close the generated holes

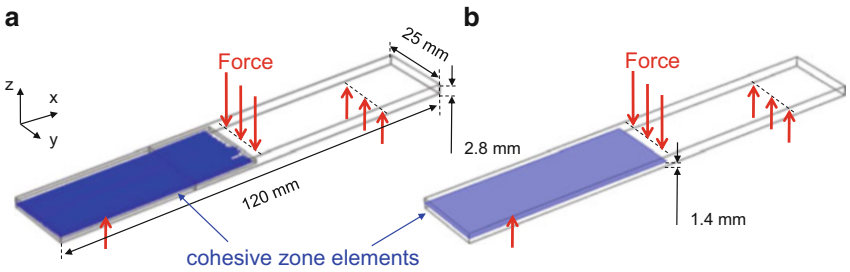

Fig. 6.52 FEM-model configuration used to calculate strain fields due to static load using extracted fracture surface (**a**) and reference case with plane fracture surface (**b**)

are being generated directly within the FEM program. From the imported crack surface, only the lower half was kept, and the remaining crack surface was joined with a surrounding volume using a sequence of intersection and union commands to yield the volume shown in Fig. 6.48. The so-obtained volume was then embedded within the full 3D geometry of a mode II specimen as shown in Fig. 6.52a. The full fracture surface of the specimen is reached by extrusion of the crack contour at the left edge of the embedded volume and finally yields the blue fracture surface seen in Fig. 6.52a. For comparison a second model with identical outer geometry is generated. As a major difference, the second model uses a simple rectangular crack representation at the half-thickness position of the laminate as seen in Fig. 6.52b.

For further computations, a line load acting in z-direction is applied at the center of the specimen, while at the position of the lower supports, displacement constraints are chosen, inhibiting movement in x-direction and z-direction. Material properties are those of Sigrafil CE1250-230-39 as listed in Table B.1 in Appendix B. The full fracture surface is modeled by cohesive zone elements following the implementation described in Sect. 4.2.

Within the "Structural Mechanics module" of COMSOL Multiphysics, the configurations of Fig. 6.52 are subject to a stationary analysis using an applied force equal to the residual load after crack growth as obtained in the experiment. The computation results are visualized as false-color plots of the shear angle in Fig. 6.53. This representation of the calculated deformation is chosen in analogy to the evaluation of mode II crack growth using DIC techniques presented in Sect. 3.4. The typical 2D image seen by a DIC system is shown as an additional inset for both cases.

It is evident from Fig. 6.53 that the different implementations of crack geometry result in noticeable differences in the computed shear angle values around the crack position and along the delaminated area. Both cases allow identifying the position of the crack tip by the steplike change in shear angle from 0° to -0.5° or less. However, the remaining signatures of the strain field around the position of the crack tip are affected by the real shape of the crack tip, causing less distinct areas of positive shear angle above and below the crack tip for the case shown in Fig. 6.53b.

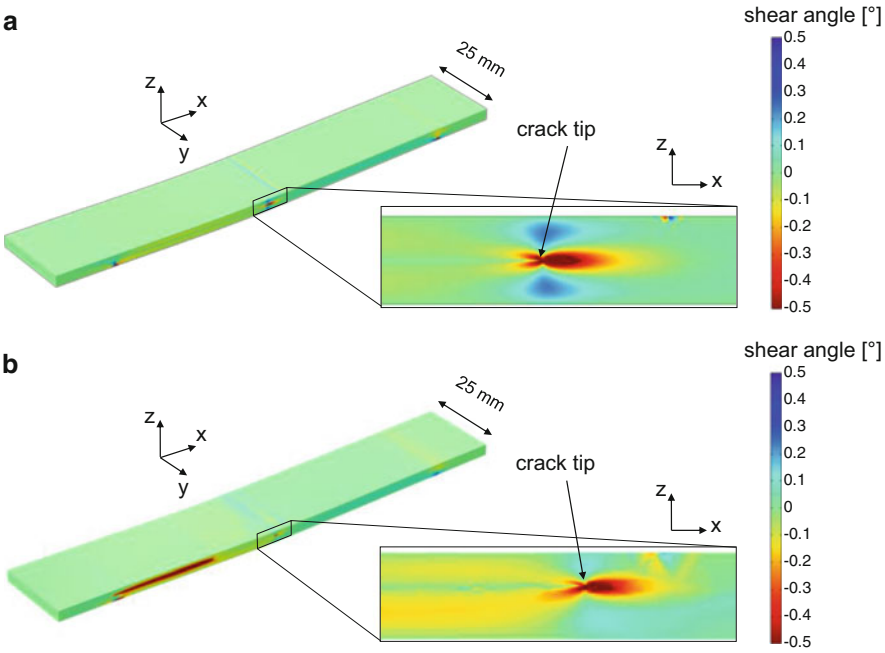

Fig. 6.53 Comparison of calculated shear angle in ENF test for laminate with perfect center crack (**a**) and shear angle due to real fracture surface as obtained from CT scan (**b**)

Moreover, the present finding is in contrast to the typical observations of crack growth by DIC methods as seen in Figs. 3.48, 3.50, and 3.51 in Sect. 3.4. Thus, it may be speculated if the shear strain signatures seen by DIC methods are really due to the deformation of the speckle pattern or are more a result of the local chipping of the speckle pattern due to interlaminar crack growth.

As second example for numerical computation utilizing an extracted fracture surface, the configuration shown in Fig. 6.54 is presented. Applying the same software environments as for the previous example, the fracture surface of a RTM6 specimen as used for flexural testing in Sect. 5.2 is extracted from a CT scan and is joined with a 3D volume of the full specimen. This test specimen is then embedded within a model of the full test setup including a 3D representation of the lower supports and the geometry of the pushrod introducing the mechanical load. The dimensions of the model as well as the selected boundary constraints are given in Fig. 6.55. To induce a mechanical load, the upper surface of the pushrod was subject to a force of 78.8 N acting in z-direction, while movement of the edges at the bottom of the support was constrained along the x-direction and the z-direction. As further boundary constraints, the extracted fracture surface was modeled by cohesive zone elements following the approach presented in Sect. 4.2 with a von Mises failure criterion and the material properties of RTM6 as given in Tables B.1 and B.4 of Appendix B.

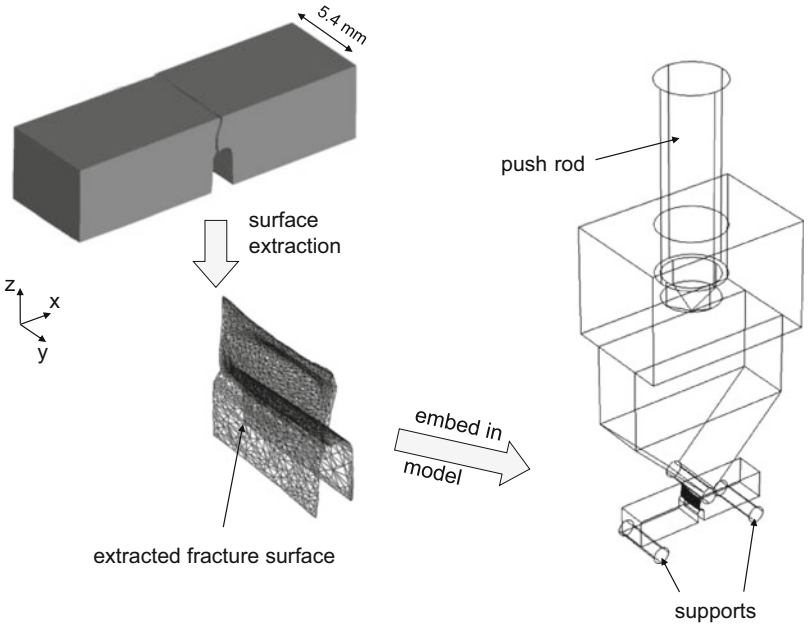

Fig. 6.54 Scheme of procedure used to transfer CT scan of fracture surface into FEM-model

Within the "Structural Mechanics module" of COMSOL Multiphysics, the configuration of Fig. 6.55 is subject to a transient analysis. The acting force was identical to the failure load of the specimen. All dimensions including the fracture plane are chosen identical to the experimentally used specimen. Based on the material properties and the von Mises failure criteria, this causes crack initiation and crack propagation at this load level.

As seen from the false-color visualization of the degradation function $\check{C}(\boldsymbol{r})$ in Fig. 6.56, the applied external load results in crack initiation at the notch position with crack growth from the bottom to the top of the specimen. The position of the crack front is determined by the evaluation of $\check{C}(\boldsymbol{r})$ and does not obey a spatially and temporally homogeneous growth. Instead, the topology of the fracture surface causes an inhomogeneous growth of the crack front along the y-axis. Due to the initial acceleration, the crack velocity increases first (cf. $t = 12.5$ µs to $t = 25.0$ µs) and decelerates when approaching the top of the specimen (cf. $t = 50.0$ µs to $t = 100.0$ µs). The dynamics of this crack growth confirm well with results of a fractographic analysis of the resultant fracture plane (cf. Fig. 5.8). Here a crack initiation zone with sliver-like pattern is observed followed by pronounced Wallner lines when reaching the deceleration zone. In order to perform a physically correct description of the dynamics of the crack growth, it is thus required to consider the topology of the fracture plane. A simple approach defining a straight rectangular plane was found to yield inaccurate results even for such relatively simple failure modes [86]. Especially the complex fracture planes of composite materials are

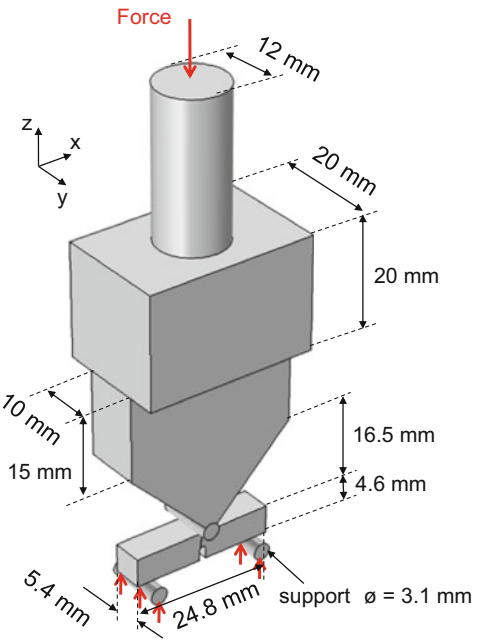

Fig. 6.55 FEM-model configuration used to calculate crack growth in flexural test configuration (based on [86])

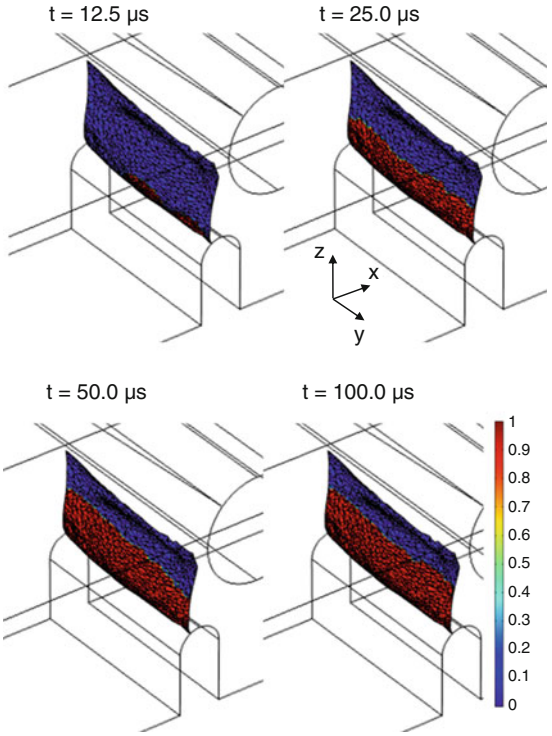

Fig. 6.56 Crack growth in RTM6 specimen as function of time visualized as false-color diagram of the degradation function $\check{C}(\boldsymbol{r})$ (based on [86])

expected to benefit from approaches to directly obtain the geometric dimensions from computed tomography measurements (see also Sect. 7.2.4.2). However, other approaches using meshless methods [87–93] or refined FEM approaches [84, 94] do not need to define an explicit fracture plane and therefore should be able to capture the dynamics intrinsically. For such advanced modeling methods, the extraction of fracture planes may be then directly be used to compare model predictions to experimental results.

6.5.2 In Situ Testing

As primary difference to the previous section, the approaches considered as in situ testing using computed tomography typically combine a mechanical test rig with a CT device as presented in Sect. 6.4. Many applications to visualize and detect damage progression in composite materials by in situ approaches have already been published [25, 26, 31, 34, 35, 40, 46–61]. Thus, the aim of this section is not to repeat their findings but to demonstrate the capabilities of such approaches using some representative examples. To this end, results of a study are presented, which investigate a subset of the fundamental microscopic failure modes of fiber reinforced composites.

In order to induce a particular failure mechanism, the load frame concept introduced in Sect. 6.3 is applied. This comprises an aluminum load frame component in combination with a PMMA tube used as load deflection. The load stage itself is a fully computer-controlled commercial device of type “Microtest” applying a 500 N load cell for precise force measurements. For later combination with AE measurements (see Sect. 7.2.4.2), the load frame was modified to form a waveguide to transfer the AE signal from the source position to the sensor position [60]. A 3D CT scan of a mounted specimen showing the details of the transfer components is found in Fig. 6.57 next to a photography image of the system. As explained in Sect. 6.3, the system applies a load deflection concept introducing tensile or compressive load by movement of the lower bar. The upper bar is mounted to the surrounding PMMA tube and acts as fixed counterpart. To improve the acoustic propagation path between the specimen and the sensor, a waveguide concept is applied, which is explained in more detail in Sect. 7.2.4.2. The AE sensor itself is mounted in a screw thread machined into the upper part of the stage.

The specimens investigated are fabricated as prepreg laminate using the carbon/epoxy system Sigrafil CE1250-230-39 following the curing cycle recommended by the manufacturer. Miniaturized samples of nominally 1.7 mm × 2.0 mm × 22.0 mm (depth × width × height) are cut from the laminates utilizing a water-cooled low-speed saw with precision diamond blade. Samples are attached to the aluminum load bars by an UHU Plus endfest 300 epoxy adhesive. Mechanical testing is carried out in displacement-controlled mode with 0.2 mm/min displacement rate.

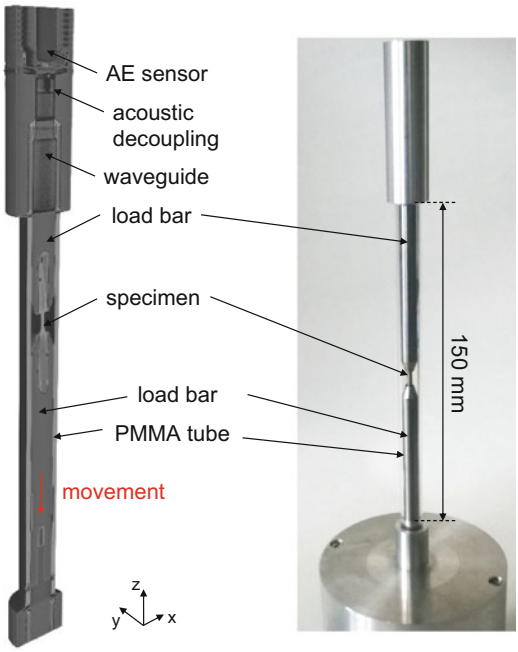

Fig. 6.57 3D scan result of load rig showing cross-section of the mounted specimen, the tensile bars, and the mounted acoustic emission sensor (*left*) and according photography image (*right*)

The generated load-displacement curves are recorded by the software program "Deben Microtest."

The different types of load bars are shown in Fig. 6.58. Depending on the intended type of load, several load bar types are used. Tension and compression tests were carried out by using the load bars of Fig. 6.58a. Here the specimen is directly bonded to the load bars by an epoxy adhesive. The large embedding length seen in Fig. 6.57 offers a comparatively large contact surface to the adhesive and is sufficient to transfer tensile or compressive loads into the specimen until failure in the free section. For compressive loading, the adhesive bonding has the further advantage to support the specimen at the edges, thus avoiding end crushing by a shear load introduction. As further load concept, a mode I configuration was realized by a wedge cracking method. This is shown in Fig. 6.58b holding the sharp wedge on the bottom load bar and a respective slit for the specimen machined into the upper load bar.

In mechanical testing, a comparatively stiff load frame should allow a direct measurement of the specimen strain by evaluation of the cross-head displacement, but the strain rate intrinsically changes during increased loading [95]. For the given case, the stiffness of the full load frame was evaluated as 635 N/mm for tensile and compressive load and was not found to be sufficiently high to evaluate the specimen strain directly from the movement of the stepper motor. A typical measurement curve for the stress-strain relationship during tensile testing transverse to the fiber

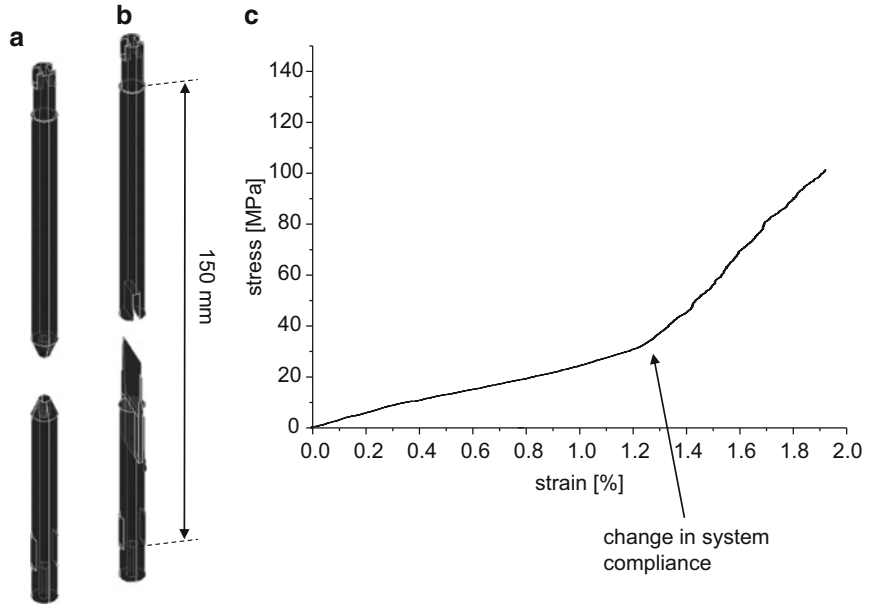

Fig. 6.58 Several load bars as used for tension and compression (**a**) and mode I (**b**) loading. Typical stress-strain curve from tensile test exhibiting change of system compliance (**c**)

direction is shown in Fig. 6.58c. As seen from the figure, the curve exhibits a characteristic change of compliance which unlikely originates from the material. Instead such changes in system compliance were found in various load configurations, being partially at characteristic load levels and partially being unique for each measurement. Consequently, a direct compensation of the load frame compliance by a linear correction factor is not possible. For this case a nonlinear compensation would be required to account for changes in system compliance, i.e., due to screw threads, bolt connections, and other connectors. Since this was found to be partially at unique load levels, no generally applicable compliance correction could be made. Therefore, further discussion will be limited to the observed failure mode and the stress level during failure.

In the following, results are shown for the occurrence of inter-fiber failure in a unidirectional composite due to tensile and compressive load as well as fiber failure due to tensile and compressive load. Further results are presented on tracking of interlaminar crack growth resulting from mode I loading. All scans were performed using a Nanotom 180 CT scanner applying the scan parameters of Table 6.5 and the "phoenix datos|*x*2 reconstruction" software for image acquisition and VGStudio MAX for postprocessing. Given the high voxel resolution, details of the fracture plane and inclusions (e.g., pores) in the bulk composite are readily visible.

Table 6.5 Acquisition parameters for CT scan

Measurement parameter	Value
Detector type	Amorphous Silicon CsI detector $(3072 \times 2400)px^2$
Filter	None
X-ray tube voltage	50 kV
X-ray tube current	170 µA
Focal spot size	0.6 µm
Voxel size	1.7–3.8 µm
Acquisition angles	1000
Image exposure time	1 s
3D reconstruction software	Phoenix datos|x2 reconstruction

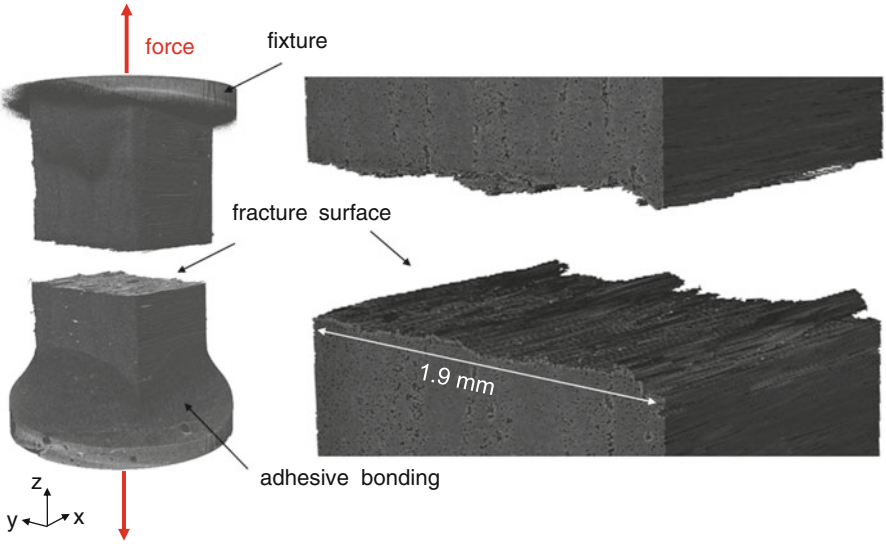

Fig. 6.59 3D scan of the failure mode due to tensile load transverse to fiber axis including details of the fracture surface (reprinted from [60])

6.5.2.1 Inter-fiber Failure

For tensile loading transverse to the fiber direction, the expected failure mode is a comparatively smooth fracture surface normal to the applied load. An exemplary CT scan after final failure of the specimen as shown in Fig. 6.59 confirms this assumption. Although the details of the fracture plane reveal a certain roughness of the fracture surface, the overall orientation is found to be normal to the load axis.

Beyond the possibility to extract the fracture surface as discussed in Sect. 6.5.1.2, the 3D capabilities of the scan allow further inspections to be made. Since failure of unidirectional composite transverse to the fiber axis is dominated by the presence of laminate imperfections (e.g., inclusions, dry spots, and resin rich

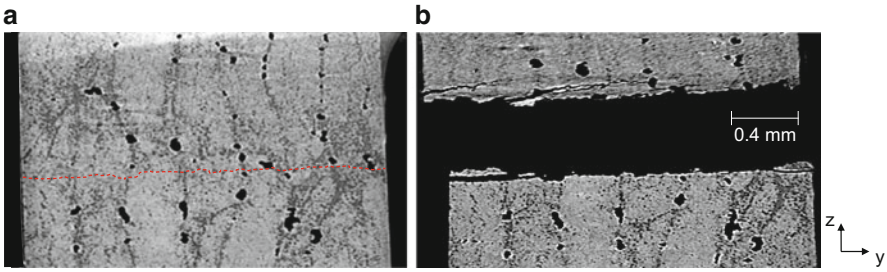

Fig. 6.60 Exemplary *yz*-cross-section before (**a**) and after failure (**b**) due to tensile load transverse to fiber axis

areas), the 3D analysis may readily be used to spot such regions and to investigate their relation to formation of the fracture plane. In the spirit of [28], an example of such inspection is shown in Fig. 6.60.

Here the scan of Fig. 6.60a reveals a substantial amount of porosity in the laminate, which has been quantified to be in the order of 5 %. From the position of the pores, it is obvious that they link and agglomerate at the positions between the individual plies, which can readily be observed in Fig. 6.60a. A direct comparison to the contour of the fracture plane shown in Fig. 6.60b can thus be made. As seen from the red line in Fig. 6.60a, the later position of the fracture surface links several pores on the right side of the specimen. However, based on the cross-section shown in Fig. 6.60, a deviation of the crack from the *y*-axis would be expected including some of the bigger pores seen in Fig. 6.60a. Instead, the crack stays almost in parallel to the *y*-axis. There are several reasons for this behavior. First, for the given load scenario, the presence of a crack tip will immediately result in transverse failure of the material due to the superimposed normal stress. Energetically it is not favorable to deviate from this angle (cf. Sect. 2.2). Unless there are strong stress concentrators, the crack will keep its propagation direction as seen in Fig. 6.59. Moreover, the specific cross-section shown in Fig. 6.60 is only a part of the full volume. Since some of the larger pores seen in Fig. 6.60a do not extend along the full dimension of the specimen along the *x*-axis, they do not necessarily constitute weak paths to dominate crack propagation.

To investigate the relation between porosity and formation of the fracture plane further, two examples of compression transverse to the fiber axis are discussed next. A direct comparison of the specimen shape before and after failure is shown in Fig. 6.61.

Based on Puck's failure theory, an angle of approximately 53° would be expected for an otherwise perfect and homogenous laminate [96, 97]. As seen from the 3D scan result in Fig. 6.61, the shape and orientation of the fracture surface in this load case does coincide well with the prediction. However, parts of the specimen were certainly subject to bending loads due to the partial or full buckling of the specimen after crack initiation. Accordingly, smaller fragments of the material have separated from the remaining specimen and are thus not included

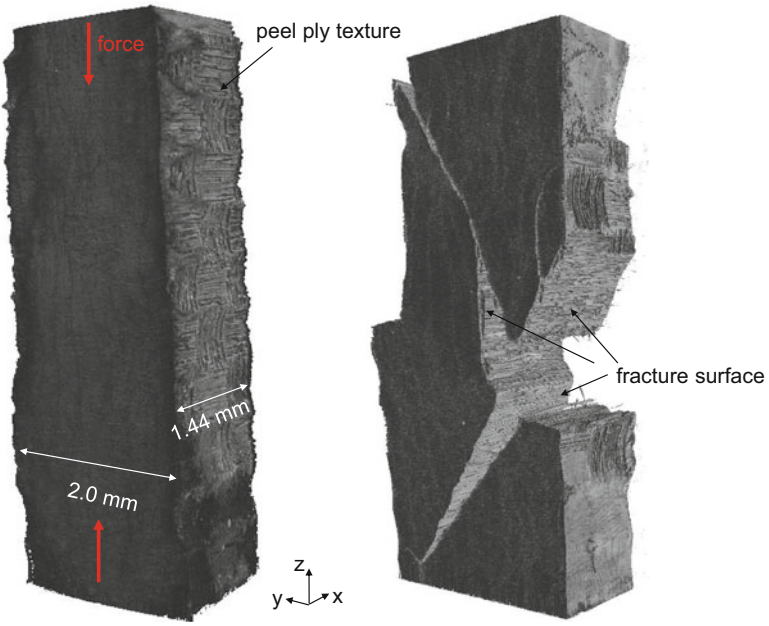

Fig. 6.61 Comparison of specimen loaded by compressive force transverse to fiber axis before and after failure

in the scan. Using an *yz*-cross-section, the resultant fracture angle can readily be measured as shown in the example of Fig. 6.62. As average of ten measurements, this evaluates as $(53.6 \pm 1.5)^\circ$ and therefore agrees well to the prediction of Puck's inter-fiber failure criterion.

To study the influence of porosity in such load cases, a relevant *yz*-cross-section of a laminate before and after fracture is shown in Fig. 6.63. The dashed line in Fig. 6.63a resembles the contour of the final fracture surface seen in Fig. 6.63b. As a result of the acting forces, a distinct fracture surface develops. This is partially due to the collapse of pores and due to multiple fractures along the paths dictated by the position of the pores. The red line of Fig. 6.63a clearly indicates that the connection of individual pores finally results in the formation of the fracture plane and thus acts as preferential path for crack growth.

6.5.2.2 Fiber Failure

In order to investigate fiber failure due to tensile and compressive load, different specimen sizes were prepared to conform with the maximum force capacity of 500 N of the used load cell. Specimens are fabricated from the Sigrafil CE1250-230-39 carbon/epoxy prepreg laminate using miniaturized samples of

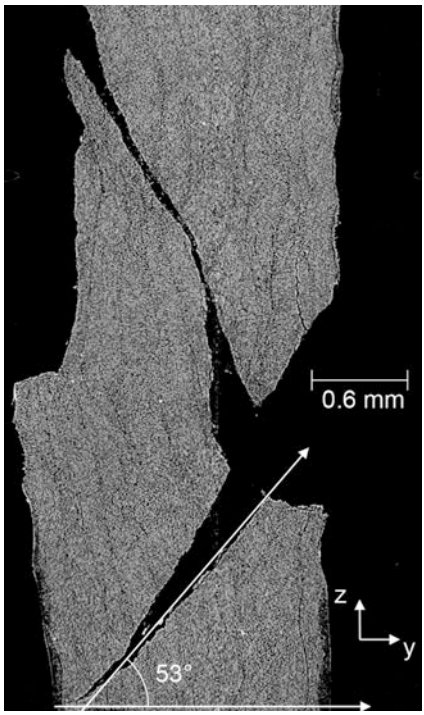

Fig. 6.62 Evaluation of fracture angle due to compressive force transverse to fiber axis

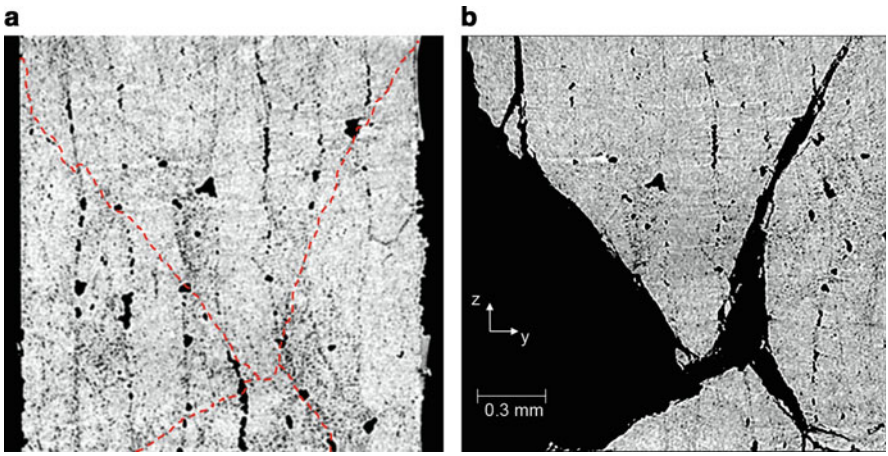

Fig. 6.63 Exemplary *yz*-cross-section before (**a**) and after failure (**b**) due to compressive load transverse to fiber axis

0.14 mm × 1.35 mm × 22.0 mm (depth × width × height). All other settings were chosen as for the previous cases.

As seen from the comparison of the specimen before and after failure in Fig. 6.64, the failure mode is distinctly different to the inter-fiber failure cases

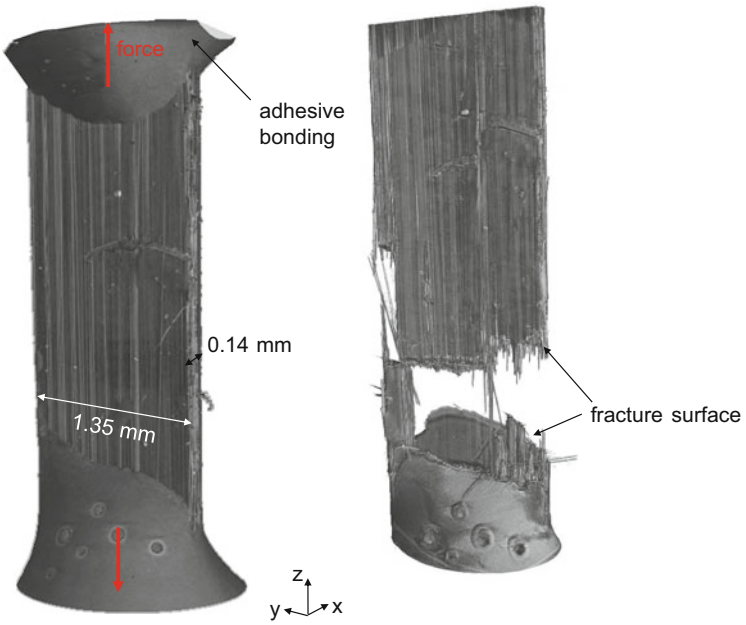

Fig. 6.64 Comparison of specimen loaded with tensile force parallel to fiber axis before and after failure

since this load configuration requires the rupture of the reinforcement fibers. Inspired by macroscopic test configurations for tensile tests parallel to the fiber axis, a tapered region as shown in the *xz*-cross-section of Fig. 6.65a was prepared using the epoxy adhesive. This ensures failure of the material in the reduced part of the specimen as seen in Fig. 6.64. In addition to the rupture of the fiber filaments, splitting along the *z*-axis occurs during failure. The latter is seen well in the comparison of the specimen cross-section in Fig. 6.65b, c. Here several inter-fiber cracks occur in parallel to the fiber axis.

The influence of pores on the occurrence of fiber filament failure has been studied in [28]. Therein it was concluded that the presence of voids increases the likelihood of a single filament fiber break in the immediate vicinity. Other experimental studies with a focus on the accumulation of single fiber filament breaks and their relevance to global failure of the laminate have provided substantial insight on this failure mode [25, 26, 56]. Moreover, substantial refinement of the theoretical framework to describe the agglomeration of fiber failure has been proposed by Swolfs et al. [98–100].

To induce failure of the specimens with compressive load applied parallel to the fiber axis, the same experimental configuration as for the tensile test is used. The taper provided by the epoxy was found to be quite useful to stabilize the specimen and to avoid buckling failure modes. As visualized the comparison of 3D scans before and after failure of the composite in Fig. 6.66, the predominant failure mode

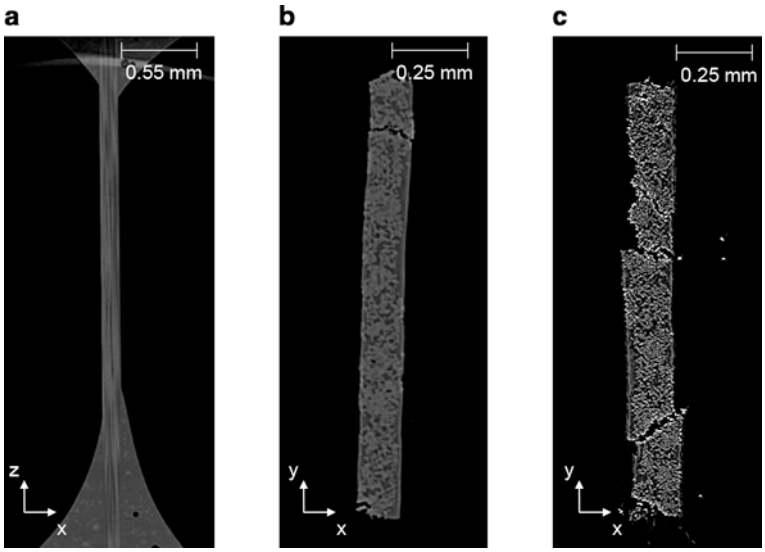

Fig. 6.65 Comparison of tensile specimen cross-section in *xz*-plane (**a**) and *xy*-plane (**b**) before loading and in *xy*-plane after loading (**c**)

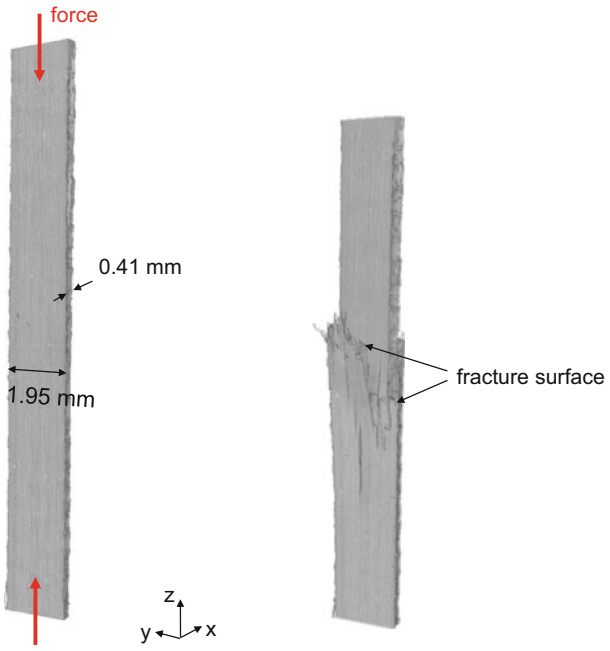

Fig. 6.66 Comparison of specimen loaded with compressive force parallel to fiber axis before and after failure

observed for the carbon/epoxy material used in this load configuration, is a brooming failure mode at the center of the specimen. This is likely induced by band kinking of the fibers prior to the final failure. As seen from the cross-sectional images in Fig. 6.67, the upper half of the specimen impacts the bottom half upon failure as typically observed in macroscopic testing. This impact causes much of the substantial damage visible in Figs. 6.66 and 6.67. The used scan resolution allows to resolve many details on the fracture mode, such as fiber fragments, the extent of delamination, splitting of the beams, and other geometrical changes. Note also the rotated alignment of the upper part of the beam compared to the bottom part. This is seen best by comparing the cross-sectional images in the *xy*-plane of Fig. 6.67 taken at the dashed red lines as indicated in the *xz*-plane cross-section.

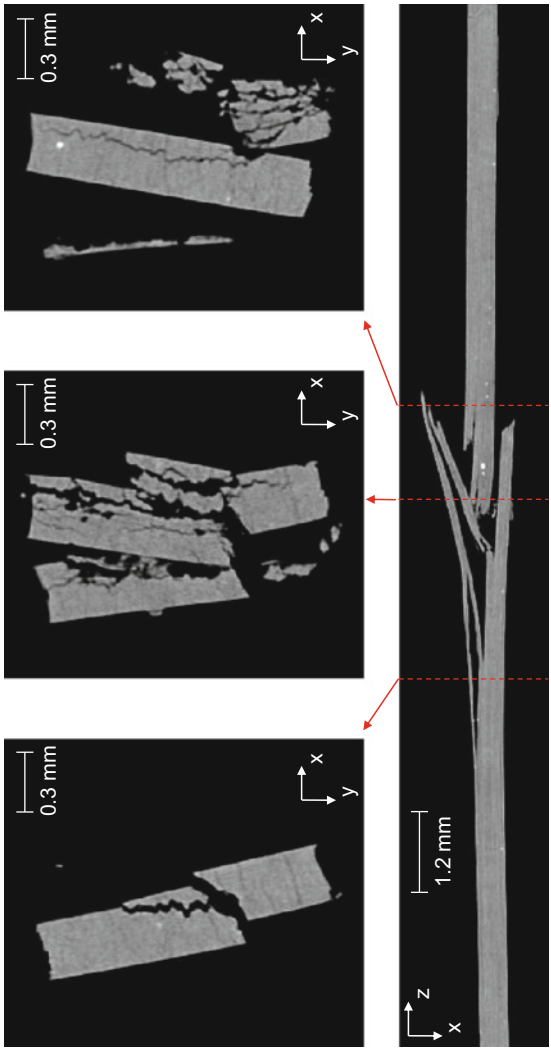

Fig. 6.67 Cross-sectional view of specimen after failure in directions perpendicular to applied load (*xy*-plane) and as cross-section aligned with applied load (*xz*-plane)

6.5.2.3 Interlaminar Failure

For initiation of an interlaminar mode I crack, a different load configuration than for tensile or compressive testing is required. As discussed in Sect. 6.3, the specimen is hold in an upright position using a fixture at the bottom part. At the top position, a sharp knife is used to induce a mode I crack due to wedge loading of the two beams. To facilitate crack initiation at the center part of the prepared specimen, a precrack is introduced prior to testing. For this test procedure, specimens are fabricated from the Sigrafil CE1250-230-39 carbon/epoxy prepreg laminate using miniaturized samples of 1.7 mm × 2.2 mm × 32.0 mm (length × width × height). The displacement rate of the indentation knife was chosen as 1 mm/min.

The resultant crack propagation after exceeding the 121 N for initiation of the precrack is shown in Fig. 6.68 for two subsequent states of knife indentation. As clearly revealed by these images, the knife indentation causes a splitting of the beam resulting in a typical mode I load condition at the position of the crack tip.

The in situ scan of this mode I crack allows examining details of the crack front, such as bifurcations or branching of the crack tip, surface roughness or interaction with particles, and voids or other defects. As an example for this kind of analysis, Fig. 6.69 presents cross-sections in the *xy*-plane (i.e., plane perpendicular to the direction of crack growth) taken at different positions along the *z*-axis. Figure 6.69a is taken at a position close to the present position of the crack tip. As noticeable from the absence of the crack on the left side of the cross-sectional image, the crack does not grow with a planar crack front along the *y*-axis (cf. also Fig. 6.44). When

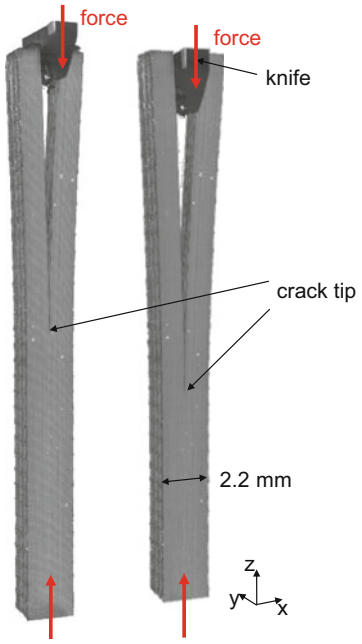

Fig. 6.68 3D visualization of interlaminar crack growth at two subsequent stages of knife indentation

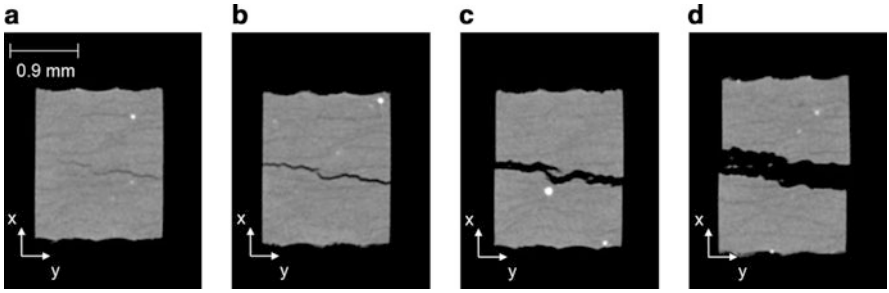

Fig. 6.69 Cross-sections in the *xy*-plane at *z*-positions of approximately 2 mm distance to the precrack

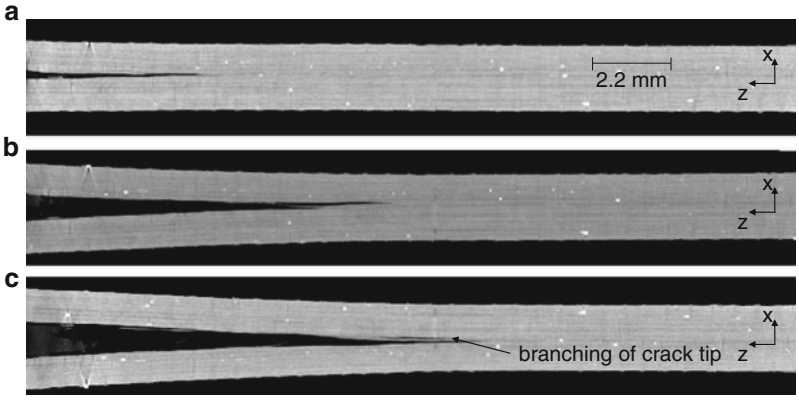

Fig. 6.70 Sequence of images in *xz*-cross-section recorded in subsequent load stages to visualize interlaminar crack propagation and branching of crack tip

moving towards the position of the indentation knife, Fig. 6.69b–d reveals the roughness of the fracture surface along the *y*-axis as well as some crack bifurcations and splitting of the laminate upon crack growth. The latter is particularly well seen for the fiber filament residues visible as small gray particles between the two fracture surfaces.

The progression of the crack tip may also be visualized for a sequence of images taken at different indentation depths of the knife. As visible in cross-sectional images in the *xz*-plane in Fig. 6.70 at identical *y*-position, the crack tip starts to propagate starting at the precrack position (Fig. 6.70a). Due to the loading of the indentation knife, the mode I condition at the crack tip causes interlaminar crack propagation at a distance of more than 3 mm ahead of the knife position. Thus, the crack is solely driven by a mode I load and is not simply cut by the indentation knife. As seen from the cross-sectional images in Fig. 6.70b, c, the crack splits the laminate and propagates with occasional branching of the crack tip. This sequential imaging mode is therefore well suited to detect influences of enclosed particles or to study deviations in the crack front due to the presence of defects, the textile architecture, or other likely crack deflectors.

References

1. Cosslett, V.E., Nixon, W.C.: X-ray shadow microscope. Nature **168**, 24–25 (1951)
2. Cosslett, V.E., Nixon, W.C.: X-ray shadow microscopy. Nature **170**, 436–438 (1952)
3. Cosslett, V.E., Nixon, W.C.: X-Ray Microscopy. Cambridge University Press, Cambridge (1960)
4. Nixon, W.C.: Improved resolution with the x-ray projection microscope. Nature **175**, 1078–1079 (1955)
5. Flisch, A., Wirth, J., Zanini, R., Breitenstein, M.: Industrial computed tomography in reverse engineering applications. In: Computerized Tomography for Industrial Applications and Image Processing in Radiology, Berlin, Germany (1999)
6. Buzug, T.M.: Computed Tomography: From Photon Statistics to Modern Cone-Beam CT. Springer, Berlin (2008)
7. Kalender, W.A.: Computed Tomography: Fundamentals, System Technology, Image Quality, Applications. Wiley, New York (2011)
8. Shull, P.J.: Nondestructive Evaluation: Theory, Techniques, and Applications. Marcel Dekker, Inc., New York (2002)
9. Radon, J.: Über die Bestimmung von Funktionen durch ihre Integralwerte längs gewisser Mannigfaltigkeiten. Berichte Sächsische Akad. der Wissenschaften. **69**, 262–277 (1917)
10. Barrett, J.F., Keat, N.: Artifacts in CT: recognition and avoidance. Radiographics **24**, 1679–1691 (2004)
11. Herman, G.T.: Fundamentals of Computerized Tomography: Image Reconstruction from Projections. Springer, Berlin (2009)
12. Brooks, R.A., Di Chiro, G.: Beam hardening in X-ray reconstructive tomography. Phys. Med. Biol. **21**, 390–398 (1976)
13. Jin, P., Bouman, C.A., Sauer, K.D.: A method for simultaneous image reconstruction and beam hardening correction. In: 2013 I.E. Nuclear Science Symposium and Medical Imaging Conference (2013 NSS/MIC), pp. 1–5. IEEE (2013)
14. Van de Casteele, E., Van Dyck, D., Sijbers, J., Raman, E.: A model-based correction method for beam hardening artefacts in X-ray microtomography. J. Xray. Sci. Technol. **12**, 43–57 (2004)
15. Van Gompel, G., Van Slambrouck, K., Defrise, M., Batenburg, K.J., de Mey, J., Sijbers, J., Nuyts, J.: Iterative correction of beam hardening artifacts in CT. Med. Phys. **38**, S36 (2011)
16. Kastner, J., Plank, B., Salaberger, D.: High resolution X-ray computed tomography of fibre- and particle filled polymers. In: 18th World Conference on Nondestructive Testing, 16-20 April 2012, Durban, South Africa, pp. 16–20 (2012)
17. Salaberger, D., Arikan, M., Paier, T., Kastner, J.: Characterization of damage mechanisms in glass fibre reinforced polymers using X-ray computed tomography. In: 11th European Conference on Non-destructive Testing (ECNDT 2014), Prague, Czech Republic, pp. 1–9 (2014)
18. Krause, M., Hausherr, J.M., Burgeth, B., Herrmann, C., Krenkel, W.: Determination of the fibre orientation in composites using the structure tensor and local X-ray transform. J. Mater. Sci. **45**, 888–896 (2009)
19. Sugimori, M., Lam, F.: Macro-void distribution analysis in strand-based wood composites using an X-ray computer tomography technique. J. Wood Sci. **45**, 254–257 (1999)
20. Little, J.E., Yuan, X., Jones, M.I.: Characterisation of voids in fibre reinforced composite materials. NDT E Int. **46**, 122–127 (2012)
21. Kastner, J., Plank, B., Salaberger, D., Sekelja, J.: Defect and porosity determination of fibre reinforced polymers by X-ray computed tomography. In: 2nd International Symposium on NDT in Aerospace, Hamburg, Germany, pp. 1–12 (2010)
22. Stoessel, R., Kiefel, D., Oster, R., Diewel, B., Llopard Prieto, L.: μ-computed tomography for 3d porosity evaluation in Carbon Fibre Reinforced Plastics (CFRP). In: International Symposium on Digital Radiology and Computed Tomography, Berlin, Germany (2011)

23. Plank, B., Mayr, G., Reh, A., Kiefel, D., Stoessel, R., Kastner, J.: Evaluation and visualisation of shape factors in dependence of the void content within CFRP by means of X-ray computed tomography. In: 11th European Conference on Non-destructive Testing (ECNDT 2014), Prague, Czech Republic (2014)
24. Kiefel, D., Stoessel, R., Plank, B., Heinzl, C., Kastner, J.: CFRP porosity characterisation using μ-computed tomography with optimized test parameters supported by XCT-simulation. In: Proceedings of Conference on Industrial Computed Tomography (iCT2014), Wels, Austria, pp. 35–43 (2014)
25. Scott, A.E., Mavrogordato, M., Wright, P., Sinclair, I., Spearing, S.M.: In-situ fibre fracture measurement in carbon-epoxy laminates using high resolution computed tomography. Compos. Sci. Technol. **71**, 1471–1477 (2011)
26. Scott, A.E., Sinclair, I., Spearing, S.M., Mavrogordato, M., Bunsell, A.R., Thionnet, A.: Comparison of the accumulation of fibre breaks occurring in a unidirectional carbon/epoxy composite identified in a multi-scale micro-mechanical model with that of experimental observations using high resolution computed tomography. In: Matériaux 2010, Nantes, France, pp. 1–9 (2010)
27. Scott, A.E., Hepples, W., Kalantzis, N., Wright, P., Mavrogordato, M.N., Sinclair, I., Spearing, S.M.: High resolution damage detection of loaded carbon/epoxy laminates using synchrotron radiation computed tomography. In: ICCM-18 18th International Conference on Composite Materials, pp. 1–6. ICC Jeju, Korea (2011)
28. Scott, A.E., Sinclair, I., Spearing, S.M., Mavrogordato, M.N., Hepples, W.: Influence of voids on damage mechanisms in carbon/epoxy composites determined via high resolution computed tomography. Compos. Sci. Technol. **90**, 147–153 (2014)
29. Allen, T., Scott, A., Hepples, W., Spearing, S.M., Reed, P.A., Sinclair, I., Testing, N., Resistance, D.: Investigating damage resistance of hybrid composite—metallic structures using multi-scale computed In: ECCM16—16th European Conference on Composite Materials, Sevilla, Spain, pp. 22–26 (2014)
30. Schilling, P.J., Karedla, B.R., Tatiparthi, A.K., Verges, M.A., Herrington, P.D.: X-ray computed microtomography of internal damage in fiber reinforced polymer matrix composites. Compos. Sci. Technol. **65**, 2071–2078 (2005)
31. Moffat, A.J., Wright, P., Buffière, J.Y., Sinclair, I., Spearing, S.M.: Micromechanisms of damage in 0° splits in a [90/0]s composite material using synchrotron radiation computed tomography. Scr. Mater. **59**, 1043–1046 (2008)
32. Moffat, A.J., Wright, P., Helfen, L., Baumbach, T., Johnson, G., Spearing, S.M., Sinclair, I.: In-situ synchrotron computed laminography of damage in carbon fibre-epoxy [90/0]s laminates. Scr. Mater. **62**, 97–100 (2010)
33. Moffat, A.J., Wright, P., Renault, A., Sinclair, I., Spearing, S.M.: Analysis of transverse ply cracks using computed tomography. In: 17th International Conference on Composite Materials, Edinburgh, UK (2009)
34. Wright, P., Moffat, A., Sinclair, I., Spearing, S.M.: High resolution tomographic imaging and modelling of notch tip damage in a laminated composite. Compos. Sci. Technol. **70**, 1444–1452 (2010)
35. Wright, P., Moffat, A., Renault, A., Sinclair, I., Spearing, S.M.: High resolution computed tomography for modelling laminate damage. In: 17th International Conference on Composite Materials, Edinburgh, UK (2009)
36. Garcea, S.C., Sinclair, I., Spearing, S.M.: Characterisation of fatigue micromechanisms in toughened carbon fiber-polymer composites using synchrotron radiation computed tomography. In: 16th European Conference on Composite Materials, Sevilla, Spain (2014)
37. Busignies, V., Leclerc, B., Porion, P., Evesque, P., Couarraze, G., Tchoreloff, P.: Quantitative measurements of localized density variations in cylindrical tablets using X-ray microtomography. Eur. J. Pharm. Biopharm. **64**, 38–50 (2006)

38. Wright, P., Fu, X., Sinclair, I., Spearing, S.M.: Ultra high resolution computed tomography of damage in notched carbon fiber—epoxy composites. J. Compos. Mater. **42**, 1993–2002 (2008)
39. Sinclair, R., Preuss, M., Maire, E., Buffiere, J.Y., Bowen, P., Withers, P.J.: The effect of fibre fractures in the bridging zone of fatigue cracked Ti-6Al-4V/SiC fibre composites. Acta Mater. **52**, 1423–1438 (2004)
40. Aroush, D.R.-B., Maire, E., Gauthier, C., Youssef, S., Cloetens, P., Wagner, H.D.: A study of fracture of unidirectional composites using in-situ high-resolution synchrotron X-ray microtomography. Compos. Sci. Technol. **66**, 1348–1353 (2006)
41. Forsberg, F., Sjödahl, M., Mooser, R., Hack, E., Wyss, P.: Full three-dimensional strain measurements on wood exposed to three-point bending: analysis by use of digital volume correlation applied to synchrotron radiation micro-computed tomography image data. Strain **46**, 47–60 (2010)
42. Forsberg, F., Mooser, R., Arnold, M., Hack, E., Wyss, P.: 3D micro-scale deformations of wood in bending: synchrotron radiation muCT data analyzed with digital volume correlation. J. Struct. Biol. **164**, 255–62 (2008)
43. Badel, P., Vidal-Sallé, E., Maire, E., Boisse, P.: Simulation and tomography analysis of textile composite reinforcement deformation at the mesoscopic scale. Compos. Sci. Technol. **68**, 2433–2440 (2008)
44. Scott, A.E., Clinch, M., Hepples, W., Kalantzis, N., Sinclair, I., Spearing, S.M.: Advanced micro-mechanical analysis of highly loaded hybrid composite structures. In: ICCM 17—17th International Conference on Composite Materials, Edinburgh, UK (2009)
45. Zauner, M., Keunecke, D., Mokso, R., Stampanoni, M., Niemz, P.: Synchrotron-based tomographic microscopy (SbTM) of wood: development of a testing device and observation of plastic deformation of uniaxially compressed Norway spruce samples. Holzforschung. **66**, (2012)
46. Stampanoni, M., Groso, A., Isenegger, A., Mikuljan, G., Chen, Q., Bertrand, A., Henein, S., Betemps, R., Frommherz, U., Böhler, P., Meister, D., Lange, M., Abela, R., Boehler, P.: Trends in synchrotron-based tomographic imaging: the SLS experience. In: Developments in X-ray Tomography V, pp. 63180M–63180M–14 (2006)
47. Groso, A., Abela, R., Stampanoni, M.: Implementation of a fast method for high resolution phase contrast tomography. Opt. Express. **14**, 8103 (2006)
48. Maire, E., Carmona, V., Courbon, J., Ludwig, W.: Fast X-ray tomography and acoustic emission study of damage in metals during continuous tensile tests. Acta Mater. **55**, 6806–6815 (2007)
49. Baensch, F., Zauner, M., Sanabria, S.J., Sause, M.G.R., Pinzer, B.R., Brunner, A.J., Stampanoni, M., Niemz, P.: Damage evolution in wood: synchrotron radiation micro-computed tomography (SRμCT) as a complementary tool for interpreting acoustic emission (AE) behavior. Holzforschung **69**(8), 1015–1025 (2015)
50. Cazaux, J., Erre, D., Mouze, D., Patat, J.M., Rondot, S., Sasov, A., Trebbia, P., Zolfaghari, A.: Recent developments in X-ray projection microscopy and X-ray microtomography applied to materials science. J. Phys. IV **03**, 2099–2104 (1993)
51. Chotard, T.J., Boncoeur-Martel, M.P., Smith, A., Dupuy, J.P., Gault, C.: Application of X-ray computed tomography to characterise the early hydration of calcium aluminate cement. Cem. Concr. Compos. **25**, 145–152 (2003)
52. Steppe, K., Cnudde, V., Girard, C., Lemeur, R., Cnudde, J.-P., Jacobs, P.: Use of X-ray computed microtomography for non-invasive determination of wood anatomical characteristics. J. Struct. Biol. **148**, 11–21 (2004)
53. Trtik, P., Dual, J., Keunecke, D., Mannes, D., Niemz, P., Stähli, P., Kaestner, A., Groso, A., Stampanoni, M.: 3D imaging of microstructure of spruce wood. J. Struct. Biol. **159**, 46–55 (2007)

54. Van den Bulcke, J., Masschaele, B., Dierick, M., Van Acker, J., Stevens, M., Van Hoorebeke, L.: Three-dimensional imaging and analysis of infested coated wood with X-ray submicron CT. Int. Biodeterior. Biodegrad. **61**, 278–286 (2008)
55. Helliwell, J.R., Sturrock, C.J., Grayling, K.M., Tracy, S.R., Flavel, R.J., Young, I.M., Whalley, W.R., Mooney, S.J.: Applications of X-ray computed tomography for examining biophysical interactions and structural development in soil systems: a review. Eur. J. Soil Sci. **64**, 279–297 (2013)
56. Scott, A.E., Sinclair, I., Spearing, S.M., Thionnet, A., Bunsell, A.R.: Damage accumulation in a carbon/epoxy composite: comparison between a multiscale model and computed tomography experimental results. Compos. Part A Appl. Sci. Manuf. **43**, 1514–1522 (2012)
57. Hu, X., Wang, L., Xu, F., Xiao, T., Zhang, Z.: In-situ observations of fractures in short carbon fiber/epoxy composites. Carbon **67**, 368–376 (2014)
58. Brault, R., Germaneau, A., Dupré, J.C., Doumalin, P., Mistou, S., Fazzini, M.: In-situ analysis of laminated composite materials by X-ray micro-computed tomography and digital volume correlation. Exp. Mech. **53**, 1143–1151 (2013)
59. Rolland, H., Saintier, N., Robert, G.: Damage mechanisms into short glass fibre reinforced thermoplastic during in-situ microtomographic tensile tests. In: ECCM16—16th European Conference on Composite Materials, Sevilla, Spain (2014).
60. Kalafat, S., Zelenyak, A.-M., Sause, M.G.R.: In-situ monitoring of composite failure by computing tomography and acoustic emission. In: 20th International Conference on Composite Materials, Copenhagen, Denmark, pp. 1–8 (2015)
61. Borstnar, G., Mavrogordato, M.N., Sinclair, I., Spearing, S.M.: Micro-mechanistic analysis of in-situ crack growth in toughened carbon/epoxy laminates to develop micro-mechanical fracture models. In: ECCM16—16th European Conference on Composite Materials, Sevilla, Spain (2014)
62. Silva, F.A., Williams, J.J., Chawla, N.: 3D Microstructure Visualization of SiC Particle Reinforced Al Matrix Composites by X-ray Synchrotron Tomography. In: ICCM 17—17th International Conference on Composite Materials, Edinburgh, UK (2009)
63. Borstnar, G., Mavrogordato, M.N., Helfen, L., Sinclair, I., Spearing, S.M.: Interlaminar fracture micro-mechanisms in toughened carbon fibre reinforced plastics investigated via synchrotron radiation computed tomography and laminography. Compos. Part A Appl. Sci. Manuf. **71**, 176–183 (2015)
64. Rodríguez Hortalá, M., Requena, G., Seiser, B., Degischer, P., Di Michiel, M., Buslaps, T.: 3D-characterization of continuous fibre reinforced composites. In: ICCM 17—17th International Conference on Composite Materials, Edinburgh, UK
65. Henne, F., Ehard, S., Kollmannsberger, A., Hoeck, B., Sause, M., Drechsler, K.: Thermoplastic in-situ fiber placment for future solid rocket motor casing manufacturing. In: SAMPE Europe SETEC 14—Efficient Composite Solutions to Foster Economic Growth, Tampere, Finland (2014)
66. Sargent, J.P.: Durability studies for aerospace applications using peel and wedge tests. Int. J. Adhes. Adhes. **25**, 247–256 (2005)
67. Martiny, P., Lani, F., Kinloch, A.J., Pardoen, T.: Numerical analysis of the energy contributions in peel tests: a steady-state multilevel finite element approach. Int. J. Adhes. Adhes. **28**, 222–236 (2008)
68. Ferracin, T., Landis, C.M., Delannay, F., Pardoen, T.: On the determination of the cohesive zone properties of an adhesive layer from the analysis of the wedge-peel test. Int. J. Solids Struct. **40**, 2889–2904 (2003)
69. Khan, M.A., Mitschang, P., Schledjewski, R.: Identification of some optimal parameters to achieve higher laminate quality through tape placement process. Adv. Polym. Technol. **29**, 98–111 (2010)
70. Reiser, M.F., Semmler, W., Hricak, H.: Magnetic Resonance Tomography. Springer, Berlin (2007)

71. Kalinina, O., Kumacheva, E.: A "core-shell" approach to producing 3D polymer nanocomposites. Macromolecules **32**, 4122–4129 (1999)
72. Zhang, Y., Ouyang, H., Lim, C.T., Ramakrishna, S., Huang, Z.-M.: Electrospinning of gelatin fibers and gelatin/PCL composite fibrous scaffolds. J. Biomed. Mater. Res. B. Appl. Biomater. **72**, 156–165 (2005)
73. Chestnut, M.H.: Confocal microscopy of colloids. Curr. Opin. Colloid Interface Sci. **2**, 158–161 (1997)
74. Franck, C., Hong, S., Maskarinec, S.A., Tirrell, D.A., Ravichandran, G.: Three-dimensional full-field measurements of large deformations in soft materials using confocal microscopy and digital volume correlation. Exp. Mech. **47**, 427–438 (2007)
75. Germaneau, A., Doumalin, P., Dupré, J.-C.: Comparison between X-ray micro-computed tomography and optical scanning tomography for full 3D strain measurement by digital volume correlation. NDT E Int. **41**, 407–415 (2008)
76. Bay, B.K., Smith, T.S., Fyhrie, D.P., Saad, M.: Digital volume correlation: three-dimensional strain mapping using X-ray tomography. Exp. Mech. **39**, 217–226 (1999)
77. Pan, B., Wu, D., Wang, Z.: Internal displacement and strain measurement using digital volume correlation: a least-squares framework. Meas. Sci. Technol. **23**, 045002 (2012)
78. Leclerc, H., Périé, J.N., Roux, S., Hild, F.: Voxel-scale digital volume correlation. Exp. Mech. **51**, 479–490 (2011)
79. Smith, T.S., Bay, B.K., Rashid, M.M.: Digital volume correlation including rotational degrees of freedom during minimization. Exp. Mech. **42**, 272–278 (2002)
80. Verhulp, E., van Rietbergen, B., Huiskes, R.: A three-dimensional digital image correlation technique for strain measurements in microstructures. J. Biomech. **37**, 1313–1320 (2004)
81. Lee, S.Y., Kim, G.W., Han, B.H., Cho, M.H.: Strain measurement from 3D micro-CT images of a breast-mimicking phantom. Comput. Biol. Med. **41**, 123–130 (2011)
82. Sutton, M.A., Orteu, J.J., Schreier, H.: Image Correlation for Shape, Motion and Deformation Measurements: Basic Concepts,Theory and Applications. Springer, Berlin (2009)
83. Toda, H.: A 3D measurement procedure for internal local crack driving forces via synchrotron X-ray microtomography. Acta Mater. **52**, 1305–1317 (2004)
84. Ferrié, E., Buffière, J.-Y., Ludwig, W., Gravouil, A., Edwards, L.: Fatigue crack propagation: in-situ visualization using X-ray microtomography and 3D simulation using the extended finite element method. Acta Mater. **54**, 1111–1122 (2006)
85. Hoppe, H.: New quadric metric for simplifying meshes with appearance attributes. In: VISUALIZATION'99 Proceedings of the 10th IEEE Visualization 1999 Conference (VIS '99), Washingto, DC, USA (1999)
86. Sause, M.G.R., Zelenyak, A.-M.: Modellierung von Schallemissionsquellen auf Basis von volumetrischen Bildinformationen. In: 20. Kolloquium Schallemission, Garmisch-Partenkirchen, Germany, pp. 1–9 (2015)
87. Guo, Y., Nairn, J.: Calculation of J-integral and stress intensity factors using the material point method. Comput. Model. Eng. Sci. **6**, 295–308 (2004)
88. Guo, Y., Nairn, J.: Three-dimensional dynamic fracture analysis using the material point method. Comput. Model. Eng. Sci. **16**, 11–25 (2006)
89. Nairn, J.: Material point method calculations with explicit cracks. Comput. Model. Eng. Sci. **4**, 649–663 (2003)
90. Guilkey, J.E., Weiss, J.A.: Implicit time integration for the material point method: quantitative and algorithmic comparisons with the finite element method. Int. J. Numer. Methods Eng. **57**, 1323–1338 (2003)
91. Więckowski, Z.: The material point method in large strain engineering problems. Comput. Methods Appl. Mech. Eng. **193**, 4417–4438 (2004)
92. Wang, B., Karuppiah, V., Lu, H., Komanduri, R., Roy, S.: Two-dimensional mixed mode crack simulation using the material point method. Mech. Adv. Mater. Struct. **12**, 471–484 (2005)

93. Tan, H., Nairn, J.A.: Hierarchical, adaptive, material point method for dynamic energy release rate calculations. Comput. Methods Appl. Mech. Eng. **191**, 2123–2137 (2002)
94. Moës, N., Belytschko, T.: Extended finite element method for cohesive crack growth. Eng. Fract. Mech. **69**, 813–833 (2002)
95. Hamstad, M.A., Gillis, P.P.: Effective strain rates in low-speed uniaxial tension tests. Mater. Res. Stand. **6**, 569–573 (1966)
96. Schürmann, H.: Konstruieren mit Faser-Kunststoff-Verbunden. Springer, Berlin (2005)
97. Puck, A., Schürmann, H.: Failure analysis of FRP laminates by means of physically based phenomenological models. Compos. Sci. Technol. **62**, 1633–1662 (2002)
98. Swolfs, Y., Verpoest, I., Gorbatikh, L.: Issues in strength models for unidirectional fibre-reinforced composites related to Weibull distributions, fibre packings and boundary effects. Compos. Sci. Technol. **114**, 42–49 (2015)
99. Swolfs, Y., Gorbatikh, L., Verpoest, I.: Stress concentrations in hybrid unidirectional fibre-reinforced composites with random fibre packings. Compos. Sci. Technol. **85**, 10–16 (2013)
100. Swolfs, Y., Gorbatikh, L., Romanov, V., Orlova, S., Lomov, S.V., Verpoest, I.: Stress concentrations in an impregnated fibre bundle with random fibre packing. Compos. Sci. Technol. **74**, 113–120 (2013)